覆蓋層對鈷鐵硼性質之影響效應

Effects of capping layers on the properties of CoFeB

國 立 清 華 大 學

材料科學工程研究所

碩士論文

指導教授：賴志煌 教授 (Prof. Chih-Huang Lai)

研 究 生：9531901 宋京瑾 (Jing-Jin Song)

中 華 民 國 九 十 七 年 六 月

誌謝

時間像是條河，儘管隨之流逝的歲月無法追回，但沿途刻劃的記憶只會逐漸加深、難以磨滅。在這清華園裡，我用六年的歲月一筆一筆地雕塑著屬於自我的回憶，並於離去前刻以這部論文為這青蔥歲月帶上句號。

回首這兩年，要感謝的人有許多，希冀能以此文傳達我內心的謝意。首先感謝在這兩年中不辭辛勞指導我的賴志煌老師，感謝您的諄諄教誨和包容，在您身上所學得的所有，將會是學生未來受用無窮的至寶。有幸加入這大家庭，有學長、學姐們給予的指導引領著我，使我免於在這學問大海中迷途。感謝允中、若帆、柏翔、夢嫻、勝煌、建新、肇謙等學長姐給予的協助與鼓勵。謝謝鑫泓、家庠、彥鈞、皓程、致嘵等學長亦師亦友的支持，讓我能在漫漫學研之路上安穩前進。

宗霖、容蔚、維晨、良瑋、武璋，各位夥伴，由於你們的陪伴，一起努力、奮鬥的日子沒有孤單。謝謝國峰、鼎碩兩位學弟，聽著我的苦水，容忍我的不穩重。加琪、偉志，希望你們能成為閃亮的新星，在個別領域中一展長才。還有各位新進的成員們，歡迎你們也祝福你們。

另外，感謝工研院的沈經理以及威全、姍意、志達等學長姐；感謝同步輻射的林博士、陳博士、張先生；感謝台大的林昭吟老師；感謝工三的岑博士、許俊等的幫忙；感謝所有協助我的人，沒有你們就沒有這部論文的產生。

最後，謝謝我的家人以及所有愛我和我愛的人，但願你們能以我為榮。

京瑾

97.08.28

Abstract

To confront the limitation of development of field-switching devices in nanometer scale is inevitable. Spintronic devices with current-induced switching can solve the difficult of the field-switching devices, and then have attracted a lot of attention.

In this study, we have focused on the capping effects on the CoFeB, which is the potential candidate of ferromagnet for the current-induced switching devices, including Gilbert damping constant and the magnetic properties of CoFeB. Gilbert damping is an important factor for the critical switching current density of spin-transfer devices. To investigate the dynamic behavior of CoFeB film, we have carried out the angle dependent FMR measurement and extracted the damping constant.

Different capping layers of Ta, Cu, MgO inserted into the interface of the half MTJ structure with various heat treatment have brought about interesting effects on the CoFeB. We apply Vibrating Sample Magnetometer (VSM), Magneto-Optical Kerr Effect Meter (MOKE), and X-ray magnetic circular dichroism (XMCD) to analyze magnetic properties. In addition, we investigate the micro-structure and composition analysis by Transmission Electron Microscope (TEM) and secondary ion mass spectrometer (SIMS).

Finally, we would get the lower damping constant at the case of $Co_{60}Fe_{20}B_{20}$/MgO/Ta and it is also found that the capping effect is relative to the phase transition and interface oxidation.

摘要

本論文致力於自旋傳輸記憶體中鈷鐵硼自由層阻尼係數之研究，並探討不同覆蓋層及退火處理對鈷鐵硼自由層磁性質與阻尼係數所造成之影響。除欲以降低阻尼係數來解決自旋穿隧電流過高的難題，更希望能分析出覆蓋層與鈷鐵硼自由層相變之間的關聯性。

我們藉由電子自旋共振儀所量得的不同外加場夾角下之鐵磁共振訊號並配合數值上的計算，進而獲得鐵磁材料的阻尼係數值。初步得到自旋幫浦效應以及介面混合是額外造成阻尼係數增加的原因之一。此外，我們利用振動樣品測磁力計(VSM)、磁光柯爾效應儀(MOKE)等來分析磁性質，並利用穿透式電子顯微鏡(TEM)、二次離子質譜儀(SIMS)來進行成分以及微結構分析。

最後，在雙氧化鎂阻絕層的結構中，我們調節上層氧化鎂厚度及退火處理溫度，來獲得相當低的阻尼係數，並歸納出上層覆蓋層對鈷鐵硼相變的引導作用對自由層的表現有莫大影響。

Contents

Figure list

Chapter 1 Introduction

Since the theoretical calibration for Fe/MgO/Fe shows fabulous magnetoresistance (MR) ratio, the MgO based magnetic tunnel junctions (MTJs) have aroused a lot of interest. Afterward the experiments demonstrate over 100% tunneling magnetoresistance (TMR) ratio in the MTJs with CoFe/MgO/CoFe. Because of its high magnetoresistance ratio, MgO-based MTJs seem to be the most promising one of candidates for applications of magnetoresistive devices, such as magnetic random access memory (MRAM) and magnetic sensor. Recently, the amorphous CoFeB is widely used in the MgO-based magnetic tunnel junctions due to its proper magnetic characters. The amorphous CoFeB can also promote the growth of MgO (002), which is very crucial for the high magnetoresistance ratio. On the other hand, both the magnetic properties and the damping constant (α) of CoFeB are critical factors for spin-transfer or field-switching devices. Especially, the damping constant is important in the spin-transfer devices. It is not only contributed to the switching current, but also influences the precession time.

In this thesis, we prepared the half-MTJ samples to investigate the properties of CoFeB free layer widely used in MTJs. We chose Cu as the inserted layer because it can suppress the spin pumping effect and achieve a low damping constant in the NiFe/Cu bilayer. The lower damping constant of Cu capping layer revealed that copper owns the smaller spin-flip rate, which makes the spins, pumped out from CoFeB, easily accumulate in the Cu and then diffuse back to CoFeB. Therefore,

the ferromagnetic precession can be preserved by the diffusion-back spins, which avoids the loss of angular momentum and the enhancement of the damping constant. According to the intrinsic current density equation, lower damping constants make the small switching current density possible. Besides, a relatively low switching current of dual-barrier MTJs was reported and the extra MgO barrier was believed to be the major factor, but a systematic study of the MgO effect is still lack. In this study, we investigate the capping layer effects on properties of CoFeB films after different annealing temperatures.

Chapter 2 Background

This chapter illustrates the background relevant to the discussions in this thesis. Section 2.1 introduces the basic principles of current- induced magnetization switching. Section 2.2 is a presentation of the characteristics of the MgO-based magnetic tunnel junction. Section 2.3 is a brief summary of previous theoretical and experimental studies on the properties of amorphous CoFeB. Section 2.4 and section 2.5 are focused on Gilbert damping constant and the method for extracting the damping term, respectively. In the section 2.6, we illustrate the features of ferromagnetic resonance (FMR).

2.1 Principles of Current-Induced Magnetization Switching

2.1.1 Introduction

Recently, the current-induced magnetization switching has come into notice because of the feasibility to solve the difficult of field-switching in the nanometer scale and its potential applications to spintronic devices[1].

Current-induced magnetization switching is the phenomenon that when electrons pass through the spin-valve structures, the polarization of the electrons would change the magnetization of the ferromagnetic layer and then induce different resistance configuration states.

2.1.2 Basic Concepts of Current-Induced Magnetization Switching

In 1996, the theoretical prediction of this effect was made independently by Slonczewski and Berger[2,3]. Fig. 2-1 illustrates the process of CIMS and the different resistance states.

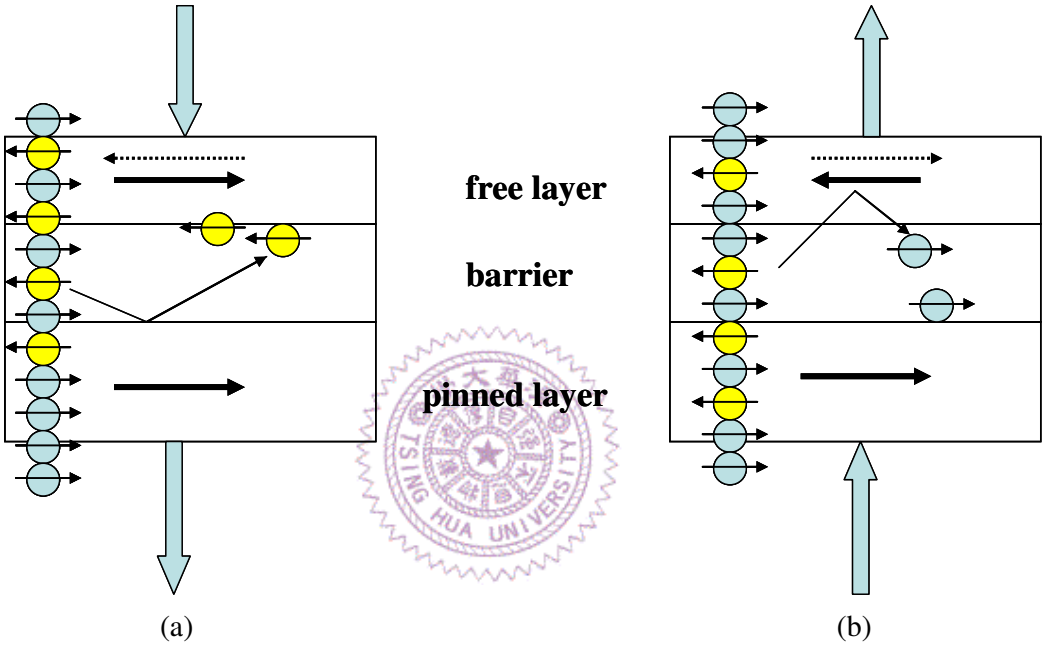

Figure 2 - 19 The schematic diagram of the CIMS process

When the current passes the free layer, the majority electrons, whose polarization is the same as that of the free layer, would cut across the barrier and arrive the side of the pinned layer, as shown in Fig. 2-1 (a). The survival majority electrons from the free layer are polarized by the pinned layer again and few minority electrons will be scattered backed to the free layer. The switching of the free layer will be induced by the accumulated scattered electrons. By this way, the parallel (low-resistance) state can be changed to the anti-parallel (high-resistance) state. On the

other hand, the anti-parallel state can be also changed to the parallel configuration state if the current enters the pinned layer first. Fig. 2-1 (b) shows that polarized electrons can switch the magnetization of the free layer.

2.1.3 A model of CIMS

The model of the CIMS current density is reported by J. Z. Sun[4], using a Stoner-Wohlfarth monodomain magnetic body to establish this model under the influence of spin transfer torque.

The intrinsic critical switching current density can be calculated from the following equation.

$$J_{c0} = \frac{2e\alpha Mst_F\left(H + H_K + 2\pi Ms\right)}{\hbar\eta} \tag{2.1}$$

where

e = electron charge

α = Landau-Lifshitz-Gilbert damping parameter

M_S = saturation magnetization

t_F = thickness of the free layer

H = applied field

H_K = effective uniaxial anisotropy field of the free layer

$\hbar$ = reduced Planck's constant

η = spin polarization factor of the incident current

In terms of the applied current, we can observe two mechanism of switching. One is fast precessional switching and the other is slow thermally-activated switching. The more completed equation of the switching current is shown as[5,6,7],

$$J_c(\tau) = J_{c0}\left[1 - \frac{k_B T}{k_u V}\ln\left(\frac{\tau}{\tau_0}\right)\right] \tag{2.2}$$

where τ_0 denotes the inverse of the activation frequency, k_u and V are functions of cell dimensions, and J_{c0} is the intrinsic critical switching current density, independent of measurement temperature and pulse width.

We can obtain $J_{c0}(\tau_0) = J_{c0}$ and use this value to compare the spin transfer efficiency no matter what the materials or structures are.

2.1.4 Reduction of CIMS switching current density

2.1.4.1 Single AlOx-based structure

The MTJ-based device with AlOx barrier made on the stacks: Ta(3)/ PtMn(20)/CoFe(2)/Ru(0.7)/CoFeB(2)/AlOx/CoFeB(2.5)/Ta(3) (unit: nm) has shown the spin transfer switching in deep-submicrometer

dimension[8]. The MR ratio of 42 % was obtained and J_{c0} is determined to be 7.8×10^6 A/cm^2.

2.1.4.2 Dual structure

The dual spin filter (DSF) structure in which an additional pinned layer was inserted on top of the free layer with magnetization antiparallel to that of the bottom pinned layer has been proposed by Yiming Huai et al[9]. The top pinned layer would induce extra spin transfer torque on the top surface of the free layer. The intrinsic switching current density J_{c0} for a DSF AlOx-based structure is 2.2×10^6 A/cm^2 and the TMR ratio is about 25%.

2.1.4.3 Single MgO barrier

MTJs with MgO barrier could derive high TMR ratio and low intrinsic switching because of high tunneling spin polarization. A MgO-based MTJ with TMR of 150% was used for CIMS, and the intrinsic switching current density J_{c0} is calculated as 2×10^6 A/cm^2 [10,11,12].

2.1.4.4 Dual MgO barrier

The dual magnetic tunnel junction structures consisting of two MgO barriers of different resistances, two pinned layers aligned antiparallel to one another, and a free layer embedded between two insulating barriers have been developed[13]. With TMR of 70%, an intrinsic switching current

density J_{c0} of 1×10^6 A/cm^2 is obtained.

2.2 Characteristics of MgO-based TMR

2.2.1 Spin Dependent Tunneling

From the results of the first-principle measurement, the large MR ratio of the MTJs with crystalline MgO barrier is due to the contribution of spin dependent tunneling[14]. The symmetry of the Bloch states in the electrodes and of the evanescent states in the barrier influences the tunnel conductance. The effects of the crystalline MgO barrier can be explained that Bloch states of different symmetry decay at different rates with this barrier, resulting in high spin polarization and huge MR ratio.

2.2.2 Materials of free layer of MgO-based MTJ

2.2.2.1 Fe

Using an amorphous AlOx barrier, the magnetic tunnel juctions exhibit a MR ratio up to 70% at room temperature[15]. This MR ratio is not high enough and seriously constrains the development of spintronic devices. However, MR ratio over 1000% is predicted in the epitaxial Fe/MgO/Fe MTJs[14,16]. In 2004, first single-crystal Fe/MgO/Fe MTJ with 180% MR ratio at 293K and 230% at 20K is experimentally demonstrated[17], as shown in Fig. 2-2.

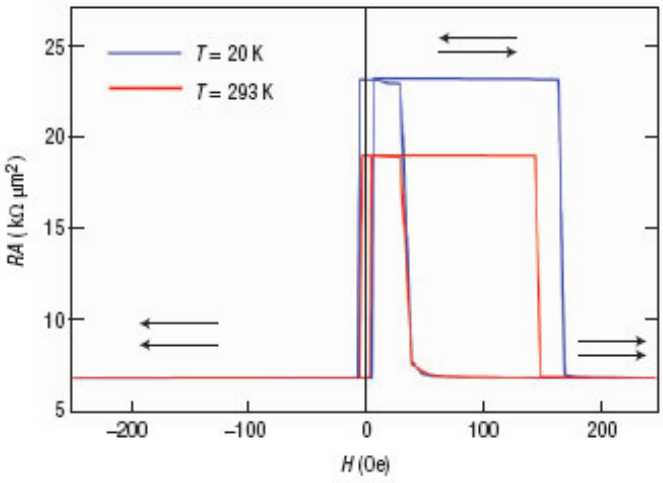

Figure 2 - 20 MR ratio of Fe(001)/MgO(001)/Fe(001) junction is 180 % at 293 K and 247 % at 20 K[17]

2.2.2.2 CoFe

Parkin et al. made changes in the free layer and also showed that the poly crystalline MTJs with highly oriented (100) MgO barrier along with $Co_{70}Fe_{30}$($Co_{84}Fe_{16}$) electrodes deposited on an amorphous TaN underlayer by in-situ shadow mask sputtering system, exhibited TMR ratio about 220% at room temperature and up to about 300% at low temperatures[18].

2.2.2.3 Co

Be explained by the band theory, an epitaxial Co/MgO/Co magnetic tunnel junction with bcc Co (001) electrodes is theoretically expected to exhibit an MR ratio even higher than that of the Fe/MgO/Fe MTJs[19]. Fig. 2-3 shows the band theory.

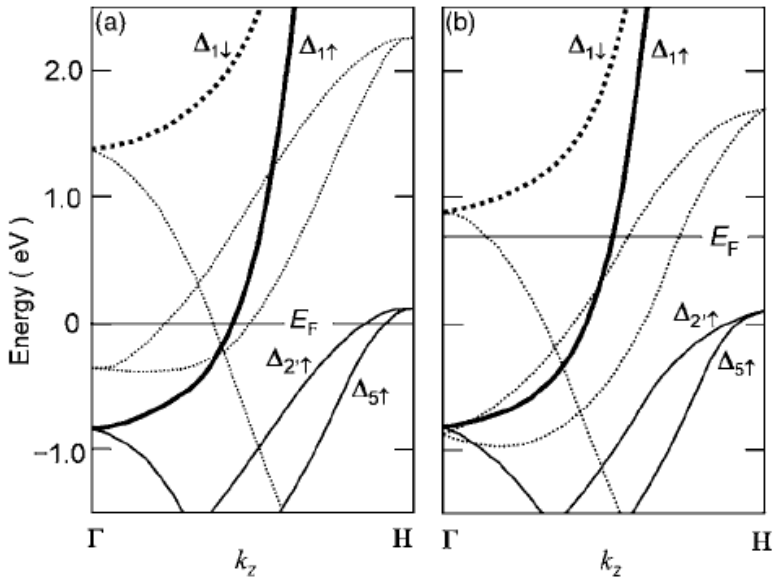

Figure 2 - 21 (a) Band dispersion of bcc Fe in the [001] direction; (b) Band dispersion of bcc Co in the [001] direction[19]

The fully epitaxial Co(001)/MgO(001)/Co(001) MTJ with metastable bcc Co(001) electrodes fabricated by molecular beam epitaxy is shown in Fig. 2-4[20]. It exhibited huge magnetoresistance ratio up to 410% at room temperature. On the other hand, temperature dependence of the MR ratio was very small compared to fully epitaxial Fe/MgO/Fe and textured CoFeB/MgO/CoFeB MTJs. However, the MR ratio of Co/MgO/Co MTJs showed larger bias voltage dependence than that of the epitaxial Fe/MgO/Fe MTJs.

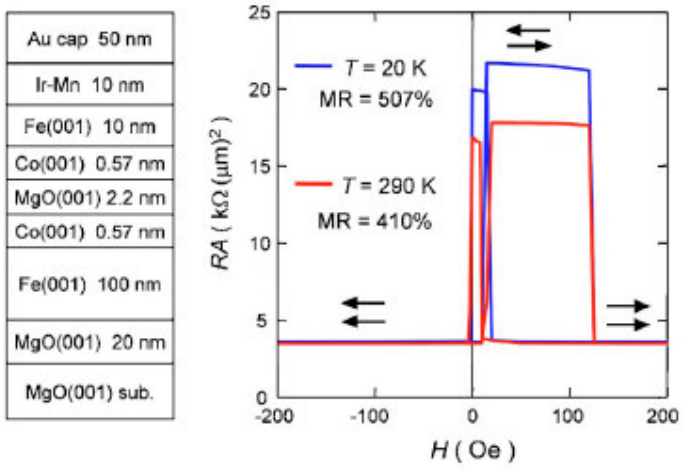

Figure 2 - 22 Structure of fully epitaxial Co(001)/MgO(001)/Co(001) magnetic tunnel junction. The MR curves at 290K and 20K are also shown[20].

2.2.2.4 Amorphous CoFeSiB and NiFeSiB

From the Stoner-Wohlfarth's single domain model, the switching field (H_{sw}) depends on the saturation magnetization (M_s) and shape anisotropy[21]. Generally, because of the lack of long-range order, amorphous metallic alloys possess[22,23]: (1) limited magnetocrystalline anisotropy, (2) high electrical resistivity, (3) nonmagnetic metalloid element to preserve glassy states and reduce M_s, and (4) low coercivity (H_c) originating from the absence of grain boundaries, precipitates, or phase segregation for pinning the domain walls.

Amorphous ferromagnetic materials like CoFeSiB and NiFeSiB appeared potential for reducing H_{sw} without reducing TMR output. The details of the experimental results in comparison with traditionally used NiFe and CoFeB free layers are listed in Table 2-1[24].

	CoFeSiB	NiFeSiB	NiFe	CoFe
Ms(emu/cc)	800	560	800	1400
Hc(Oe)	6	4	2	54
TMR ratio	28 %	30 %	19 %	36 %

Table 2 - 1 Comparison of amorphous free layers with NiFe and CoFe

2.2.2.5 Full-Heusler Alloy

Full-Heusler alloys with a chemical form of X_2YZ($L2_1$ structure) are consist of fcc sublattices occupied by the three kinds of atoms and also have B_2 and A_2 structures depending on their site disorder. The lattice structure of $L2_1$ structure of full-Heuseler alloys is shown in Fig. 2-5. The spin polarization of this alloy has been believed to be sensitive to the site disorder[25].

Some of full-Heusler alloy have been predicted to be the half metal even at room temperature because of their high Curie temperatures[26]. The large TMR values reported are listed in Table 2-2.

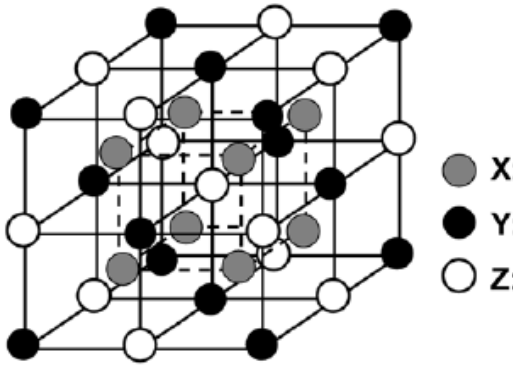

Figure 2 - 23 The $L2_1$ crystal structure with composition X_2YZ[25]

Heusler alloy	Pinned layer	Room temp.	Low tmp.	Barrier	Reference
Co2MnSi	Co70Fe30	33 %	86 % (10 k)	AlOx	Apl 85, 79(2004)
Co0.2Cr0.6Fe0.4Al	Co50Fe50	42 %	74 % (55 k)	MgO	JJAP 44, L521(2005)
Co2MnSi	Co2MnSi	67 %	570 % (2 k)	AlOx	Apl 88, 192508(2006)
Co0.2Cr0.6Fe0.4Al	Co50Fe50	90 %	240 % (4.2 k)	MgO	Apl 88, 262503(2006)
Co2MnSi	Co75Fe25	70 %	159% (2 k)	AlOx	JJAP 44, L1100
[Co2MnSi/Co2FeSi]	Co50Fe50	39 %	114% (17 k)	AlOx	Apl 89, 162506 (2006)
Co0.2Cr0.6Fe0.4Al	Co50Fe50/NiFe	16 %	26.5% (5 k)	AlOx	JJAP 42, L419(2003)
Co2MnSi	Co50Fe50	90 %	192% (4.2 k)	MgO	Apl 89, 192505(2006)
Co2FeAl0.5Si0.5	Co75Fe25	76 %	106% (5 k)	AlOx	Apl 89, 112514(2006)
Co2MnGe	Co50Fe50	14 %	70% (7 k)	MgO	Apl 99, 08A904(2006)

Table 2 - 2 Summary of the full-Heusler alloys

2.3 Properties of amorphous CoFeB

2.3.1 Growth and Crystallization Processes

After a higher MR ratio of 230% at room temperature has been demonstrated in spin-valve type MTJs with MgO barrier layer sandwiched by amorphous COFeB ferromagnetic layers[27], this free layer of CoFeB has attracted a lot of attention. By the HRTEM shown in Fig. 2-6, they found that the interfaces between CoFeB and MgO layers were very sharp and the morphology of the MTJs was smooth. After high temperature annealing, the MgO layer, grown on the amorphous CoFeB, shows a good crystalline structure with (001) texture. Compared with Fig. 2-7, the interface between MgO and CoFe layers looks rough and may be due to the mismatch of the texture for both layers.

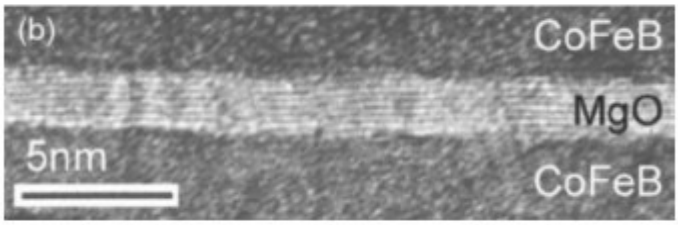

Figure 2 - 24 HRTEM image of CoFeB/MgO/CoFeB MTJs[27]

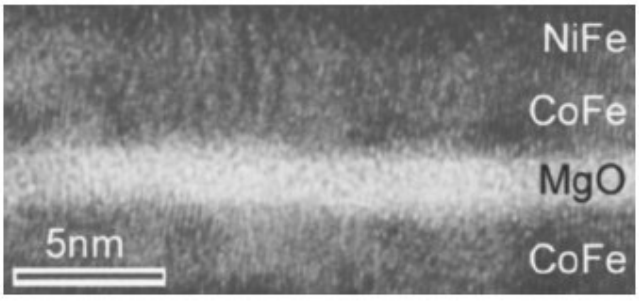

Figure 2 - 25 HRTEM image of CoFeB/MgO/CoFeB/NiFe MTJs[27]

By annealing, an amorphous CoFeB layer grown on MgO(001) crystallize in a body-centered-cubic structure with (001) orientation because MgO(001) acts as a template to crystallize CoFeB. In addition, the fact that CoFeB crystallizes in an fcc structure without any template layer means that fcc is a stable crystal structure.

Y.M. Lee et al.[28] proved the fact the MgO barrier acts as a template for crystallization of CoFeB layers, as shown in Fig. 2-8. Besides, the Ru spacer between the CoFe and CoFeB layers can not only prevent seeding from the bottom CoFe layer but also lead to a formation of MgO barrier with rock salt (001) texture.

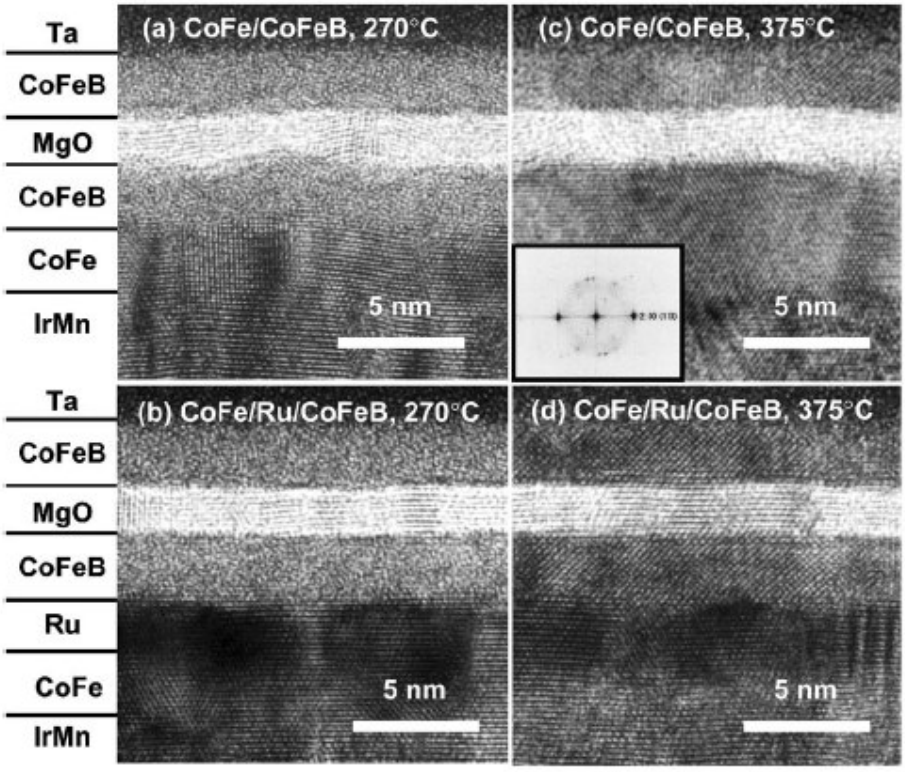

Figure 2 - 26 Cross-section HRTEM images of MTJ with the CoFe/CoFeB (S-MTJ) pinned layer and the CoFe/Ru/CoFeB pinned layer. S-MTJ after annealing at 270℃ (a) and 375 °C (c). MTJ after annealing at 270 °C (b) and 375 °C (d)[28]

2.3.2 Annealing Effect vs. TMR

The compositional change of the MgO barrier in CoFeB/MgO/CoFeB junctions has been studied by XPS depth profile[29]. J.Y. Bae et al. found that the Fe-ozide was formed at the interface of the bottom electrode and the MgO barrier at the as-deposited state but disappeared after annealing. That is because the boron has no solubility in CoFe so it diffuses into the MgO barrier side and formed boron-oxide, inducing reduction of the iron-oxide. A cleaner interface and/or the reduction of iron-oxide can increase the polarization and reach higher TMR ratio in the CoFeB/MgO/CoFeB junctions[30]. J. Hayakawa et al.[31] compared the TMR ratios of the pseudo spin valve (P-SV) and exchange-biased spin valve (EB-SV) with a MnIr antiferromagnetic layer after annealing, and the results are shown in Fig. 2-9. The TMR ratios for EB-SV are found to drop after annealing over 450^{o}C. The energy dispersive x-ray analysis shown in Fig. 2-10 also shows that annealing at 450^{o}C induce inter-diffusion of Mn and Ru atoms into the MgO barrier and ferromagnetic layers in EB-SV MTJs. The P-SV without a MnIr layer can enhance TMR ratio after high temperature annealing because of the absence of the inter-diffusion of Mn and Ru atoms.

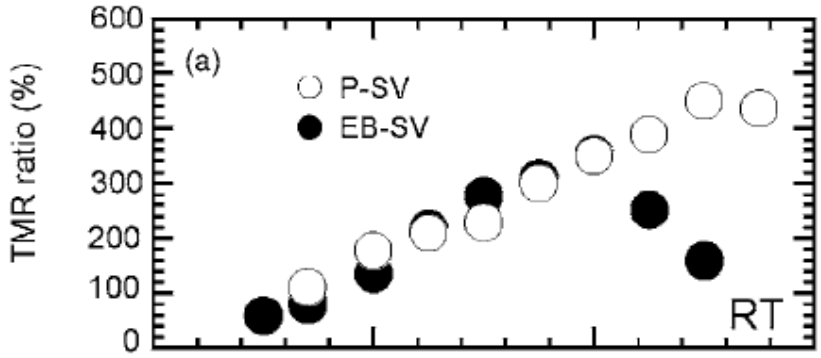

Figure 2 - 27 TMR ratios as a function of annealing temperature for PSV and ES-SV[31]

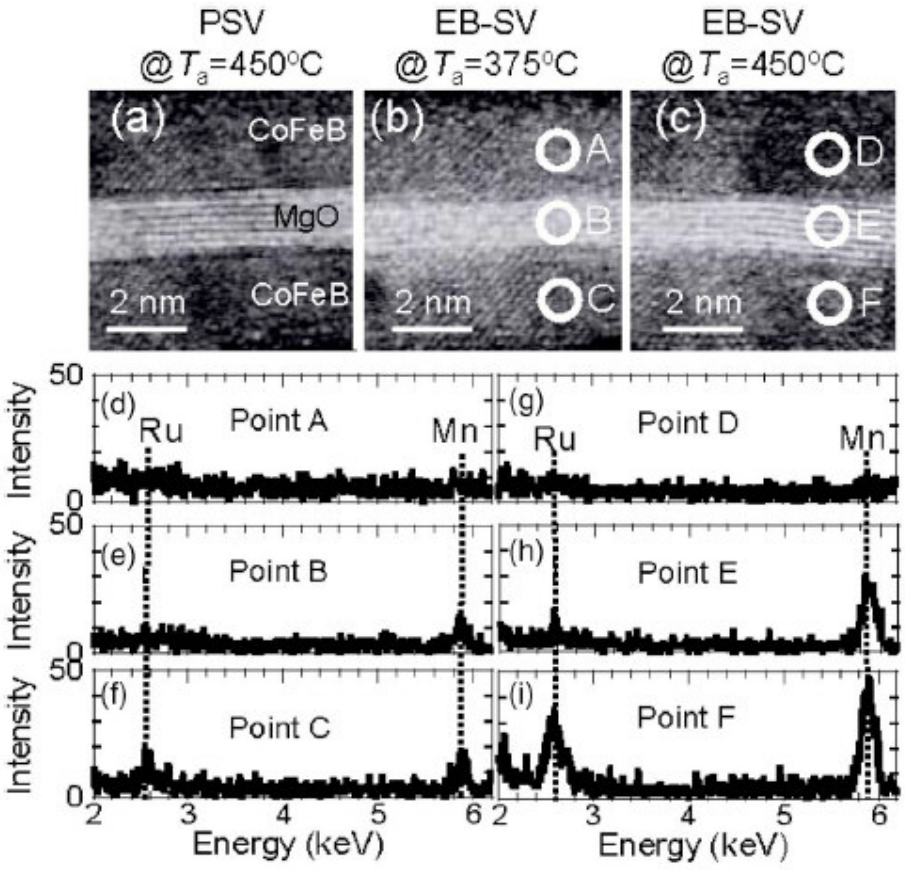

Figure 2 - 28 EDX spectrum profiles of points shown in (b) and (c) for EB-SV annealed at 375 °C [(d)-(f)] and 450 °C [(g)-(i)][31]

2.3.3 Chemical Composition vs. Microstructure

CoFeB starts to crystallize at the interface with MgO with the (001) out-of-plane texture during annealing through the in-plane 45° rotational epitaxial relationship[32], as shown in Fig. 2-11. The template effect on crystallization was reported by Yuasa et al. on the basis of reflection high-energy electron diffraction (RHEED) observation[33]. It is suggested that the polycrystalline nature of MgO restricts the lateral span of epitaxial crystallization into its own lateral grain size at the interface, which is referred to as grain-to-grain epitaxy. The chemical composition of CoFe affects the lattice match at the interface due to the lattice constant change[32].

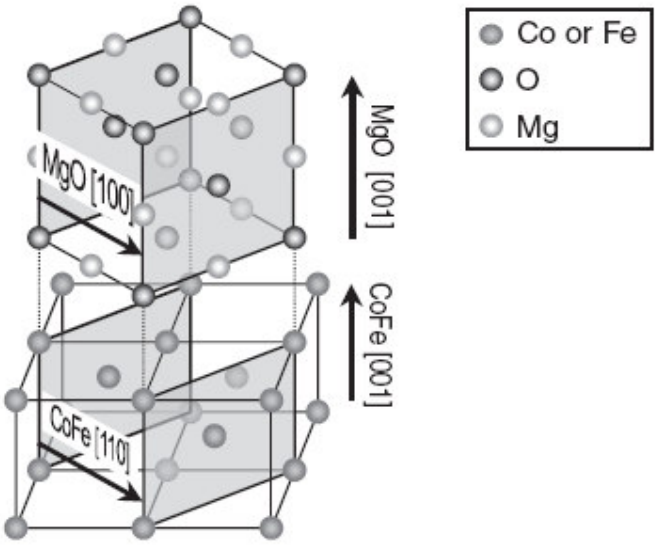

Figure 2 - 29 Schematic diagram of 45° rotational relationship between bcc CoFe and rock-salt structure MgO[32]

The d spacing of crystallized bcc Co_xFe_{100-x} in the $(Co_xFe_{100-x})_{81}B_{19}$ reference layer (RL) and MgO deposited on the $(Co_xFe_{100-x})_{81}B_{19}$ reference layer (RL) is a function of Co concentration shown in Fig. 2-12.

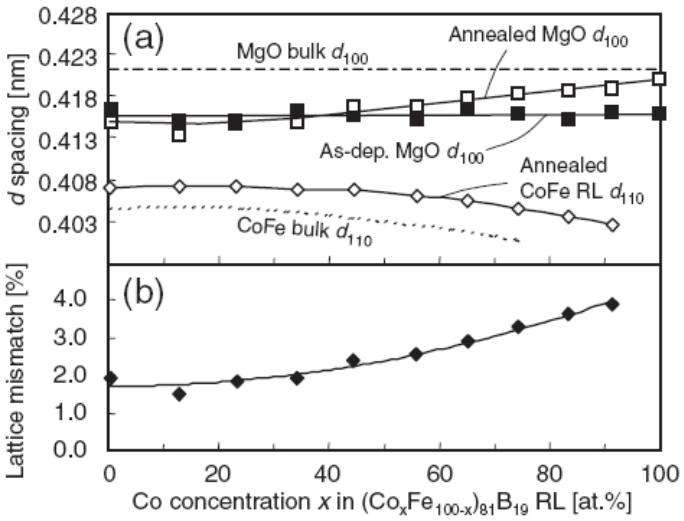

Figure 2 - 30 (a) d spacing and (b) lattice mismatch as a function of Co concentration[32]

2.3.4 Chemical Composition vs. Magnetostriction

The magnetostriction is defined as that when the ferromagnetic material is exposed to an external magnetic field, its dimensions changes. The definition and the general symbol are given by $\lambda = \Delta l / l$.

The dependence of magnetostriction on the boron concentration for the $(Co_{90}Fe_{10})_{100-x}B_x$ and $(Co_{90}Fe_{10})_{100-x}B_x$ /$Ni_{83}F_{E17}$ free layer is shown in Fig. 2-13[34], and λ of $(Co_{75}Fe_{25})_{80}$ B_{20} is also shown for reference. λ was found to be positive for all the samples. λ is about 5×10^{-6} for x= 0 at.% in the $(Co_{90}Fe_{10})_{100-x}B_x$ free layer. It drastically increases with increasing B concentration, reaches a maximum value about 2×10^{-5} for x= 15 at.%, and then rapidly drops to 4×10^{-6} for x=20 at.%. In the bi-free layer case, a NiFe layer on top of the CoFeB layer substantially reduces λ.

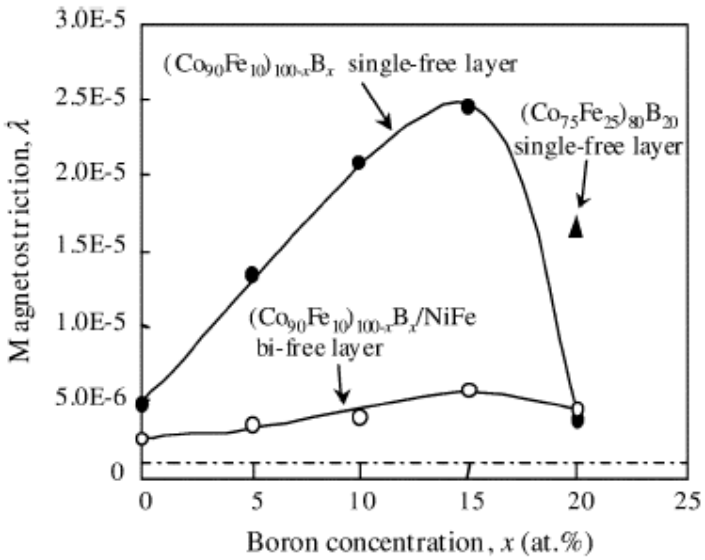

Figure 2 - 31 Dependence of magnetostrictionλon B concentration (x) of single-free layer and bi-free layer[34]

2.3.5 Chemical Composition vs. Gilbert Damping Constant

The damping constant α is determined by ferromagnetic resonance (FMR). Figure 2-14 shows the damping parameters of Co-Fe-B alloy films with various compositions[35]. The damping parameter of Co-Fe-B films slightly increased with increasing B concentration up to 30 %.

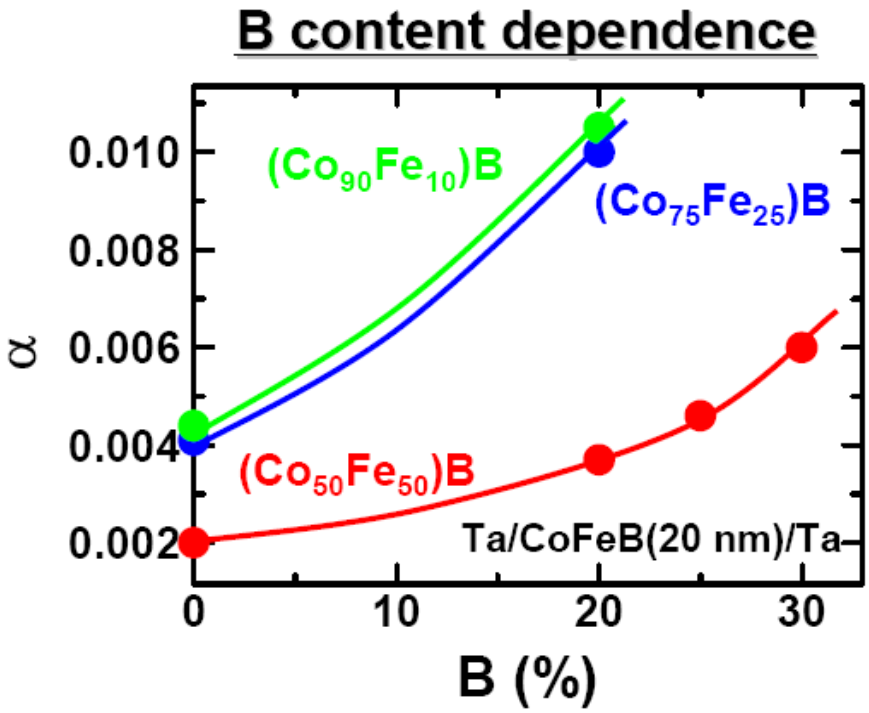

Figure 2 - 32 Estimated damping constant values for CoFeB films with various compositions[35]

2.4 Gilbert damping

2.4.1 Introduction

The time necessary to reserve the magnetization in ultrathin magnetic films and nanostructures is a central issue concerning the use of such structures within magnetic sensors and devices. The time scale for magnetization reversal is controlled by the magnetic damping of the magnetization vector **M** as it precesses about the equilibrium direction. The dynamic response of **M** is described by the Landau-Lifshitz-equation of motion[36]:

$$\frac{1}{\gamma}\frac{\partial \mathbf{M}}{\partial t} = -(\mathbf{M} \times \mathbf{H}_{\mathbf{eff}}) + \frac{G}{\gamma M_s^2}(\mathbf{M} \times \frac{\partial \mathbf{M}}{\partial t}) \qquad (2.3)$$

The first term in the right describes precession of **M** in the effective fields and the damping behavior is illustrated by the latter term. All damping mechanisms are incorporated in the Gilbert damping parameter G. Investigating the effects influencing this parameter can acquaint us with comprehension of damping mechanisms.

2.4.2 Gilbert damping vs. flux rise time of write head fields

The maximum data rate in magnetic recording depends on the achievable flux rise time. The achievable flux rise time is limited by the time required to saturate the pole tips of the magnetic write head. Takano[37] investigated the magnetization dynamics in recording heads using a finite element micromagnetic solver for the entire head structure, and the results showed that the Gilbert damping influences the flux rise time.

Suess et al.[38] simulated the head field strength and the rise time by the finite element model and understood that flux rise time increases with decreasing Gilbert damping constant. Small differences in the local field will create phase coherence which in turns slows down the time to saturation. The results of Fig. 2-15 show that large values of the Gibert damping constant are preferable for fast flux rise times.

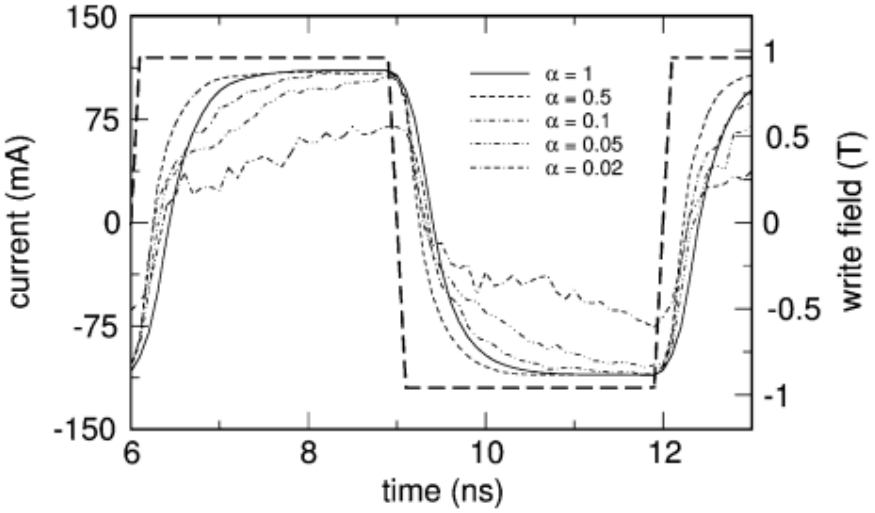

Figure 2 - 33 Head field strength for different Gilbert damping constants within the head[38]

2.4.3 Damping constant in spin torque driven perpendicular MRAM

The reliance on the shape anisotropy of the MRAM elements for memory state retention causes the switching field to be highly sensitive to any geometric and/or physical variation on the edges of the elements. An alternative design to remove the dependence is the perpendicular MRAM design in which the magnetization is perpendicular sustained by material intrinsic magneto crystalline anisotropy[39].

However, recent experimental study has shown that relatively large current density is required for switching a storage layer that is composite structure, consisting of a relatively thick layer with perpendicular anisotropy and a relatively thin layer with high spin polarization. Large damping constant has been suggested as the cause of the required current

density[40,41,42].

Fig.2-16 shows the dynamic trajectory of the volume averaged magnetization in the composite storage layer for three different values of damping constant[43]. A current with a step-function rise time is assumed for all three cases with current density of 3×10^8 A/cm^2. We can observe that with little damping constant the magnetization reversal can occur in this low current density.

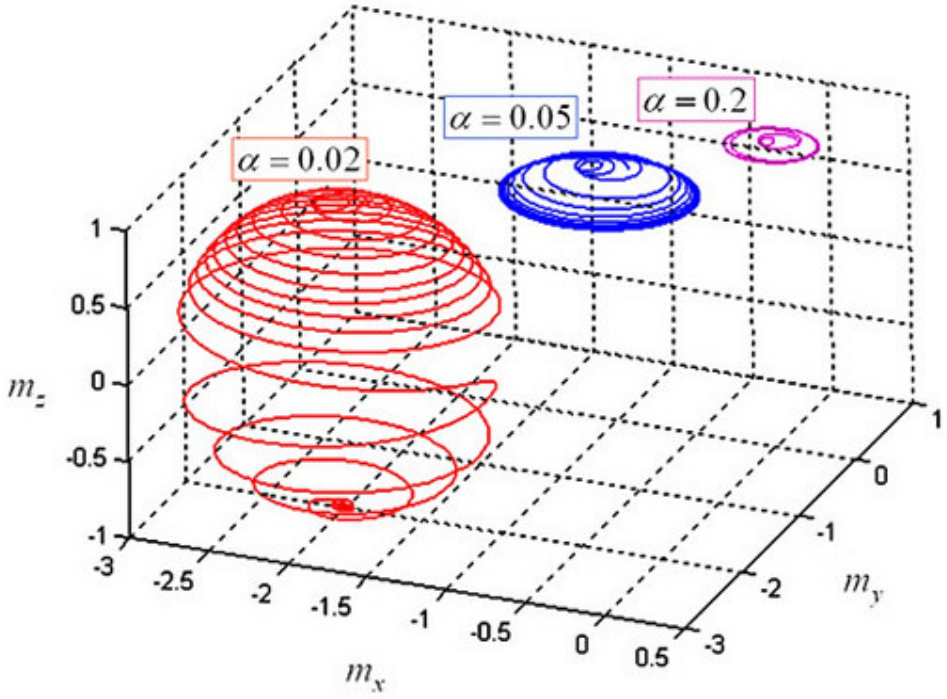

Figure 2 - 34 Calculated magnetization trajectory of the composite storage layer[43]

It is found that magnetization reversal of the perpendicular storage layer occurs when the lateral precession frequency reaches the ferromagnetic resonance condition. To reach the required precession frequency, a higher current density is required for a great value of damping constant of the perpendicular layer.

2.4.4 Influence of eddy currents on the effective damping parameter

The influence of eddy currents on magnetization dynamics may be incorporated into standard micromagnetic by the use of an effective damping parameter, as originally proposed by Chikazumi[44]. Mayergoyz et al.[45] presented a self-consistent numerical solution of the magnetic diffusion equation and the Landau-Lifshitz equation for linearly and circularly polarized applied magnetic fields and showed the effect of eddy currents for different conducting ferromagnetic films. Suess et al.[46] presented a three-dimensional micromagnetic model that includes eddy current effects and a method to calculate the effective damping parameter as a function of particle size and electric conductivity for dingle-domain particles. It shows that the diffusion of the field is linearly dependent on the conductivity and quadratically dependent on the size.

If the external field is high the magnetic field by the currents becomes negligible. On the other hand the time for magnetization reversal decreases with increasing external field. By increasing the particle size the critical transition length from homogeneous to inhomogeneous magnetization reversal is reached. The magnetic field created by the eddy current becomes nonuniform, resulting in an incoherent spin structure resulting in a vanishing eddy current contribution to damping of less than 1%. The effect of the size of the system on the eddy current contribution has shown that the increase of the particle size results in an increase of the eddy current contribution.

2.4.5 Enhancement of the Gilbert damping due to spin pumping

The Gilbert damping constant is an important parameter for spin electronics since the critical current density of CIMS is proportional to the Gilbert damping constant[41,47] and fast-switching time magnetization reversal is achieved for a large Gilbert damping constant[48]. Several mechanisms intrinsic to ferromagnetic materials, such as phonon drag[49] and spin-orbit coupling[50], have been proposed to account for the origin of the Gilbert damping constant. In addition to these intrinsic mechanisms, Mizukami et al.[51,52] and Tserkovnyak et al.[53,54] showed that the Gilbert damping constant in a nonmagnet (N)/ferromagnet (F)/nonmagnet (N) trilayer system is enhanced due to spin pumping. The enhancement of the Gilbert damping constant depends not only on the precession angle θ of the magnetization of a free layer but also on the angle ρ between the magnetization of the fixed layer and the precession axis[55]. The condition to be satisfied to realize strong enhancement of the Gilbert damping constant is $\theta=\rho$ or $\theta=\pi-\rho$.

2.5 Methods for extracting damping constant

2.5.1 Ferromagnetic Resonance

Griffiths[56] and Kittel[57] first observed the ferromagnetic resonance (FMR) by experiment, and established the initial theory of this phenomenon. Nowadays, the ferromagnetic resonance technique is

extensively used to determine the static and dynamic magnetic properties of ultrathin films. The static magnetic properties such as g-factor, anisotropy constant, and interlayer coupling of the multilayer can be estimated from the peak position of FMR spectra. Furthermore, the peak-to-peak linewidth of FMR can extract the damping constant and obtain the structural and magnetic quality[58].

2.5.1.1 Out-of-plane FMR[59]

The coordinate system used for this analysis of the angular dependence of FMR is shown as Fig.2-17. H, M and h are the vector of the DC magnetic field, magnetization and the small oscillating magnetic field of the microwave, respectively. $\theta_{H(M)}$ and $\Phi_{H(M)}$ are the polar and azimuthal angles of the DC magnetic field (magnetization).

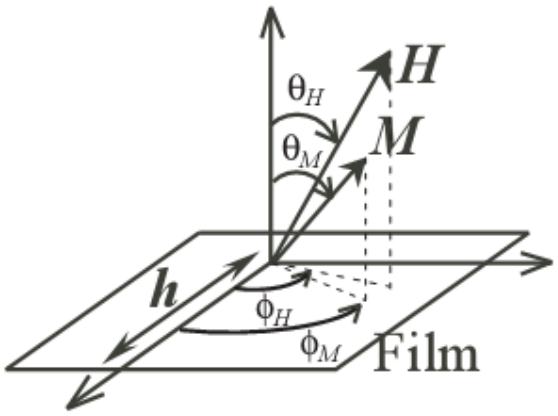

Figure 2 - 35 Schematic illustrations of the coordinate system used in the analysis of out-of plane FMR

The total energy per unit volume of magnetization of the film is modeled by

$$E = - MsH [\sin\theta_H \sin\theta_M \cos(\Phi_H-\Phi_M) + \cos(\theta_H-\theta_M)] + 2\pi Ms^2\cos2\theta_M - K_{\perp}\cos^2\theta_M \quad (2.4)$$

where the first, second and the third terms means the Zeeman energy, the demagnetization energy and the perpendicular anisotropy energy, respectively.

The resonance field (H_R) of the FMR spectrum is determined by resonance condition, which is generally given by,

$$\left(\frac{\omega}{\gamma}\right)^2 = \frac{1}{(Ms\sin\theta_M)^2}\left(E_{\theta_M\theta_M}E_{\phi_M\phi_M} - E_{\theta_M\phi_M}^2\right) \quad (2.5)$$

ω: angular frequency of microwave

M_s: saturation magnetization

γ: gyromagnetic ratio and $\gamma = g\mu_B/\hbar$,

g: g-factor,

μ_B : Bohr magnetization,

$\hbar$: Plank constant.

θ_M on resonance is determined by solving the following equation numerically,

$$\sin(2\theta_M) = (2H_R / 4\pi M_{eff.})\sin(\theta_M-\theta_H), \quad (2.6)$$

and $\Phi_M=\Phi_H$.

Here, $4\pi M_{eff.}$ is the effective demagnetization field expressed as

$4\pi M_{eff.} = 4\pi Ms - H_{\perp}$ (2.7)

$H_{\perp}=2K_{\perp} / Ms$ is the perpendicular anisotropy field.

The following set of equation can be obtained,

$$\left(\frac{\omega}{\gamma}\right)^2 = H_1 \times H_2 \tag{2.8}$$

$H_1=H_R \cos(\theta_H-\theta_M) - 4\pi M_{eff.} \cos^2\theta_M$ (2.9)

$H_2=H_R \cos(\theta_H-\theta_M) - 4\pi M_{eff.} \cos 2\theta_M$ (2.10)

H_R as a function of θ_H is calculated numerically using eqs. (2.6)-(2.10) with the parameters of $4\pi M_{eff.}$ and g-factor.

The peak-to-peak linewidth due to the intrinsic damping of magnetization precession of the FMR spectrum is given by the general formula[60],

$$\Delta H_{pp}^{\alpha} = \frac{1}{\sqrt{3}}\alpha\left(H_1 + H_2\right)\left|\frac{d\left(\frac{\omega}{\gamma}\right)}{dH_R}\right|^{-1} \tag{2.11}$$

The magnitude of the distribution of H_R from inhomogeneities, ΔH_R, is approximately expressed as[61],

$$\Delta H_R = \Delta H_R^{4\pi M_{eff.}} + \Delta H_R^{\theta_H} \tag{2.12}$$

Here,

$$\Delta H_R^{4\pi M_{eff.}} = \left|\frac{dH_R}{d\left(4\pi M_{eff.}\right)}\right| \Delta\left(4\pi M_{eff.}\right) \tag{2.13}$$

and

$$\Delta H_R^{\theta_H} = \left|\frac{dH_R}{d\theta_H}\right|\Delta\theta_H \tag{2.14}$$

However, ΔH_R should be considered to be equal to an inhomogeneous linewidth for an integrated FMR spectrum. The measured spectra are found to be almost Lorentzian in the study, hence we assume that the peak-to-peak linewidth due to ΔH_R can be express as,

$$\Delta H_{pp}^{inhomo.} = \left(1/\sqrt{3}\right)\Delta H_R \tag{2.15}$$

and then the total ΔH_{pp} can be written as the sum of ΔH_{pp}^{α} and $\Delta H_{pp}^{inhomo.}$. Through this method, we can get the damping constant α.

2.5.1.2 Frequency dependent FMR

From LLG equation shown as,

$$\frac{1}{\gamma}\frac{\partial M}{\partial t} = -(M\times H_{eff}) + \frac{G}{\gamma M_s^2}(M\times\frac{\partial M}{\partial t}) \tag{2.3}$$

The time-derivative $\frac{\partial M}{\partial t}$ in the Gilbert term produces a FMR linewidth linear in the resonance frequency ω[62],

$$\Delta H_{Glib}(\omega) = 1.16\frac{\omega G}{\gamma^2 M_s} \tag{2.16}$$

By changing the frequencies, the linear dependence of the linewidth and frequency would be extracted. Using eq. (2.16), we can get the Gilbert damping parameter.

2.5.2 Ultrafast optical excitation/ pump-probe[63]

Following excitation by the pump beam, the magnetization and magnetic anisotropy of the film undergo an ultrafast modification. For a small amplitude uniform precession, the magnetocrystalline anisotropy is assumed to be instantaneously reduced by the optical pumping. The Kerr rotation has the form:

$$\Phi_k \propto \Delta\Phi \cos(2\pi f_0 t + \Psi)\exp(-t/\tau) \tag{2.17}$$

Φ_k : Kerr rotational angle

f_0: precession frequency

τ : decay time

Ψ : phase

in the limit α<<1, we can use the equations:

$$\Delta\Phi = \frac{-\frac{1}{2}\sin[4(\Phi-\Phi_4)]\Delta(K_1/Ms}{H\cos(\Phi)+(K_1/2Ms)\cos[4(\Phi-\Phi_4)]} \tag{2.18}$$

$$f_0 = \frac{1}{2\pi}|\gamma|(H_\alpha H_\beta)^{\frac{1}{2}} \tag{2.19}$$

$$\tau = \frac{2}{|\gamma|(H_\alpha + H_\beta)\alpha} \tag{2.20}$$

$$H_\alpha = H\cos(\Phi) + \frac{K_1}{2Ms}\{3 + \cos[4(\Phi - \Phi_4)]\} + 4\pi Ms \tag{2.21}$$

$$H_\beta = H\cos(\Phi) + \frac{2K_1}{Ms}\cos[4(\Phi - \Phi_4)] \tag{2.22}$$

to get the damping constant.

2.5.3 Complex susceptibility measurement[64]

The damping parameter can be deduced from the measurements of the frequency and field dependence of the complex magnetic susceptibility, $\chi(\omega,H)=\chi'(\omega,H)-i\chi''(\omega,H)$. From the equation:

$$x = \frac{\gamma^2 g^2(1+\alpha^2)}{\omega_0^2 - \omega^2 + i\omega\Delta\omega}[l^2(F_{\theta\theta} + \frac{i\omega\alpha M}{\gamma g(1+\alpha^2)})$$
$$+ s^2(\frac{F_{\varphi\varphi}}{\sin^2\theta_0} + \frac{i\omega\alpha M}{g\gamma(1+\alpha^2)}) + 2ls\frac{F_{\theta\varphi}}{\sin\theta_0} \tag{2.23}$$

If we get the susceptibility at ferromagnetic resonance, from the relation of the ferromagnetic resonance frequency and maximum absorption frequency:

$$f_{res} = f_{\max}\sqrt{\frac{1+\alpha^2}{1-\alpha^2}} \tag{2.24}$$

We can get the damping constant.

2.6 Investigation of ferromagnetic resonance

2.6.1 Introduction

Ferromagnetic resonance (FMR) has been a well established technique to determine anisotropies in ferromagnetic (FM) systems for more than 50 years[65]. Due to its sensitivity, FMR has been successful applied to ultrathin metallic films[66]. FMR can also be used to study the coupling between FM films separated by non-magnetic spacer layers, which can be metallic or non-metallic[67]. Another important quantity can be addressed by FMR is the g value, which in solids becomes a tensor quantity. These quantities which characterize static magnetic properties are estimated from the resonance peak positions of FMR spectra. From the FMR linewidth, we can obtain the damping parameter for magnetization precession and information regarding magnetic inhomogeneity involved in films.

2.6.2 FMR in ultrathin ferromagnets

2.6.2.1 FMR in single ultrathin films

Since the energy associated with microwave absorption lies in the μK range, FMR is the technique of choice to investigate the thermodunamic ground-state properties. However, the peak-to-peak linewidth is consist of homogenrous and inhomogeneous terms. As we mentioned in the

previous paragraph, the peak-to-peak linewidth due to intrinsic damping on magnetizaton precession of the FMR can reflected the contribution from damping and we can extract this intrinsic damping term. From the change of the FMR linewidth, we can also study the homogeneity of the film. The inhomogeneous term of the FMR linewidth can show the distribution of $4\pi M_{eff}$ related to the fluctuation of the thickness in the film[68]. From :

$$\Delta(4\pi M_{eff}) = \left|\frac{d(4\pi M_{eff})}{d(d_{ferr})}\right| \delta_{ferr} \tag{2.25}$$

where δ_{ferr} is the magntidue of fluctuation of the ferromagnet thickness in a film, we assumeδ_{ferr} independent of the ferromagnet thickness and by fitting the $\left| d(4\pi M_{eff})/d(d_{ferr}) \right|$ to the experimental $4\pi M_{eff}$ vs d_{ferr} we can get the fluctuation of the ferromagnet thickness.

2.6.2.2 FMR in coupled ultrthin films[69]

A trilayer consisting of two magnetic layers which are separated by a paramagnetic spacer layer is the simplest case for studying the interlayer coupling parameter. The coupling energy U_{ex} of the two films 1 and 2 is via the term

$$U_{ex} = -J_{inter} \frac{\overrightarrow{M_1}.\overrightarrow{M_2}}{M_1 M_2} \tag{2.26}$$

After introducing the coupling term one gets from the Smit and Beljers method

$$\left(\frac{\omega}{\gamma}\right)^4 - b\left(\frac{\omega}{\gamma}\right)^2 + c = 0 \qquad (2.27)$$

The constants b and c are related to the anglae depence of the energy for coupled system, and combinning that with the FMR signals we can get the interlayer coupling parameter.

On the other hand, from the positions of optical mode and acoustic mode we would know whether the coupling is ferromagnetic (FM) or anti-ferromagnetic (AFM) illustrated in Fig.2-18.

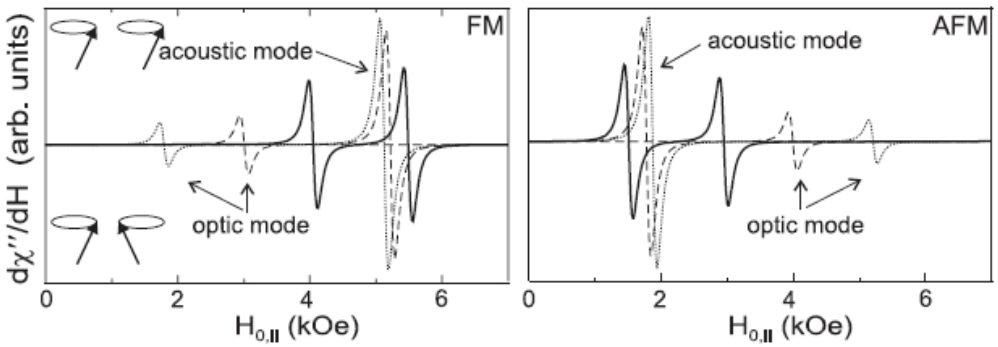

Figure 2 - 36 2-18 FMR spectra for FM and AFM coupling[69]

Chapter 3 Experimental and Analysis Technique

This chapter describes experimental techniques and analysis equipments used in the later chapters of this thesis.

3.1 Experimental Flow Chart

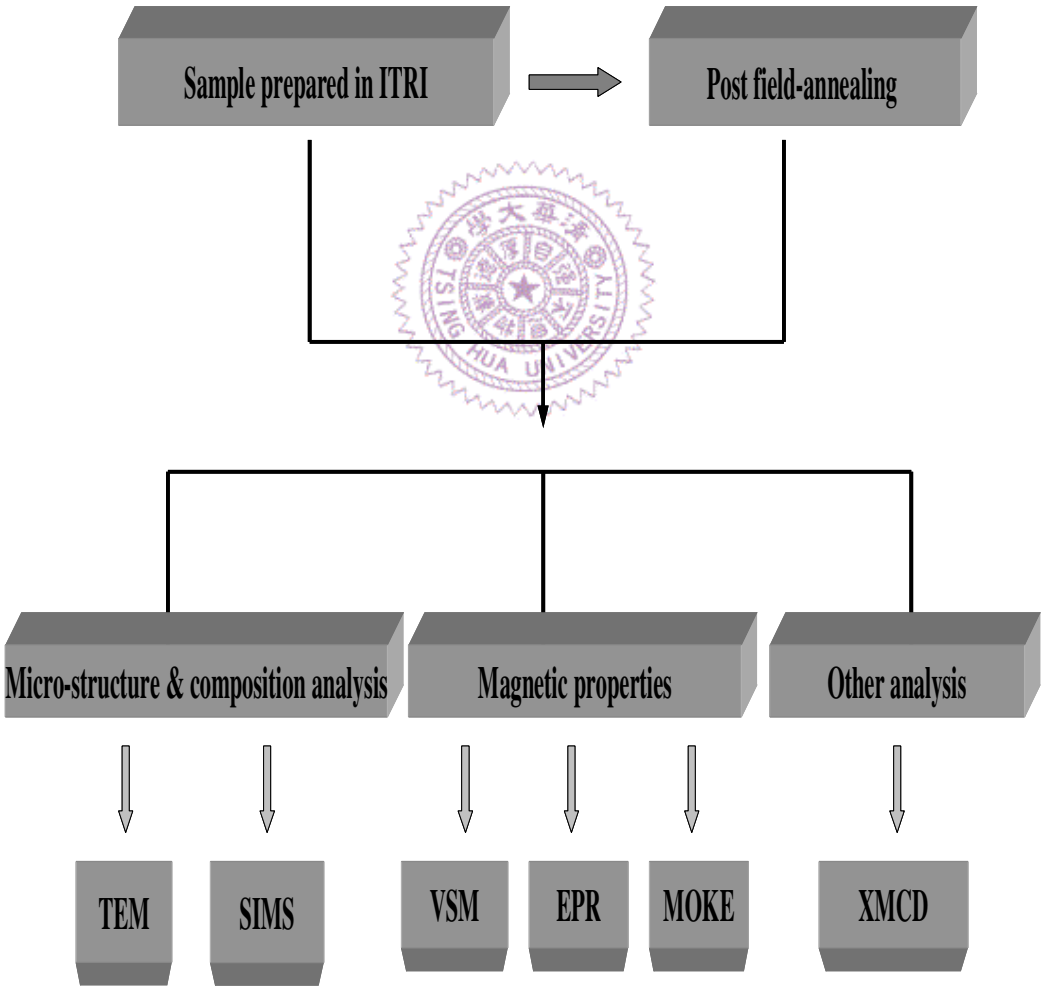

3.2 Post Field-Annealing System

A home-made field-annealing system is shown in Fig. 3-1. The samples were annealed in the base pressure down to 5×10^{-5} Torr by the mechanical and diffusion pumps. An external field about 1500 Oe applied during annealing is put near the sample so that the easy-axis of the sample can be established and the crystallization of the material occurs. The annealing temperature can be set on the heating controller.

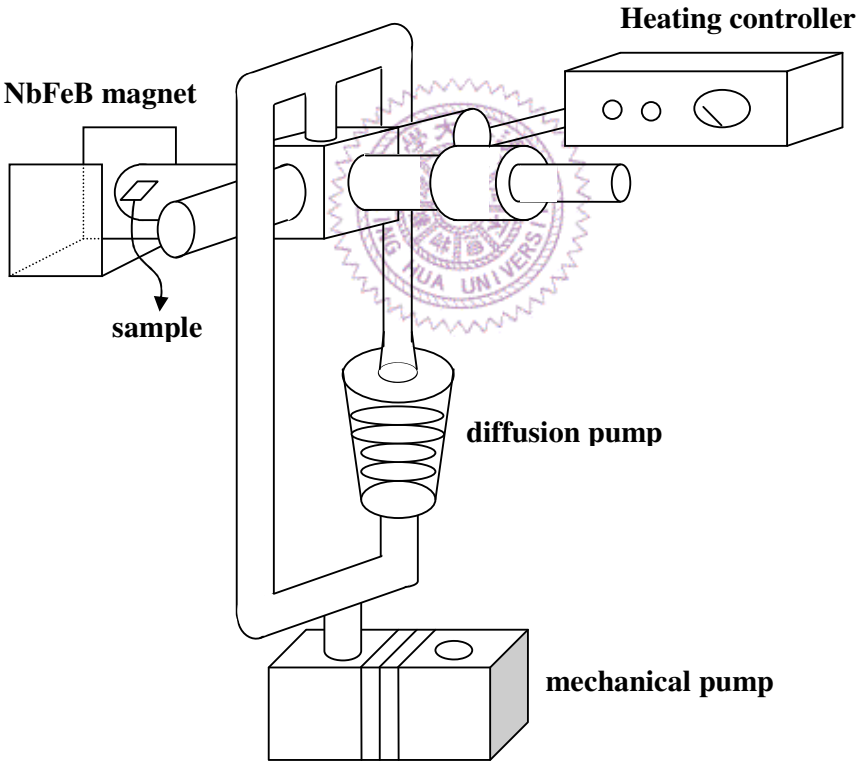

Figure 3 - 8 Field-annealing system

3.3 Vibrating Sample Magnetometer (VSM)

The measurement method was proposed by Foner. A standard vibrating sample magnetometer possesses an electromagnet to supply DC field, detecting coils to sense the variation of the magnetic flux with time, and a test rod connecting the loudspeaker and the sample.

In the beginning with measuring, the testing rod vibrates together with sample with 80Hz frequency. The direction of vibration is perpendicular to the magnetic field. An induced electromotive force (EMF) would be occurred in the coils due to the variation of magnetic flux though the detection coils. A reference sample fixed at the testing rod vibrating together with the measured sample, there is also an induced electromotive force formed in the reference coils. The different voltage between the two sets of coils is proportional to the magnetic moment of the sample. We can obtain the magnetic moment of measured sample by comparing the induced electromotive force in the detection coils with reference coils (the saturation moment Ms is known). The performance of the VSM on the sensitivity can detect the variation of the magnetization to 5×10^{-5} erg/Oe, and the maximum limit of the applied magnetic filed should be up to 20000 Oe. The scheme of VSM is shown in Fig. 3-2 and Fig. 3-3.

Figure 3 - 9 Vibrating sample magnetometer (VSM)

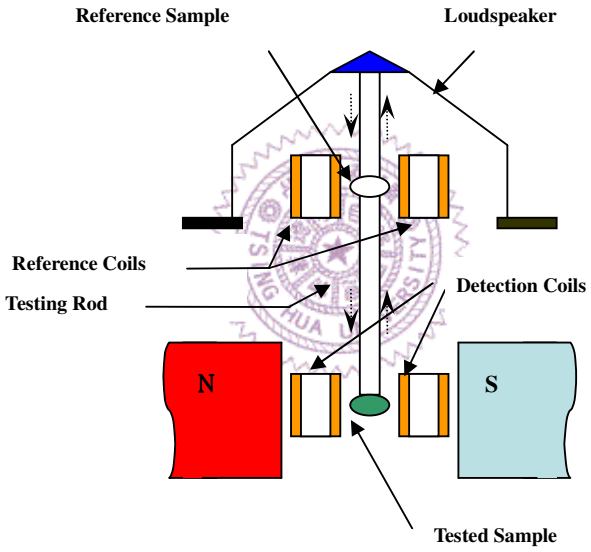

Figure 3 - 10 Schematic illustration of VSM

3.4 Magneto-Optical Kerr Effect Meter (MOKE)

Changing the rotation of the linear polarized light beam during reflection from a magnetized specimen is the principle of so called MOKE. The amount of rotation depends on the direction and magnitude

of the magnetization relative to the plane of incidence of the light beam.

As shown in Fig. 3-4, the linear polarized He-Ne laser light by a polarizer is introduced into the sample located at the center of the electromagnet. If the sample is magnetized by the field, the induced magnetization of the sample would change the dielectric constant tensor of the sample form diagonal-only form to the non-diagonal form. This complex tensor would interact with the linear polarized light, and the reflected light from the sample thus has the elliptical polarization. One can tune the magnetization of the sample by controlling the applied field to change the ellipticity and the tilted angle of the elliptical reflected light from the sample. In our setup, the reflected light is guided into another linear polarizer called analyzer, and then into a photo-diode. Theoretically, the photo-diode voltage induced by the reflected light, called the Kerr intensity, is proportional to the magnetization of the sample. Therefore, we can measure the hysteresis loop of the sample.

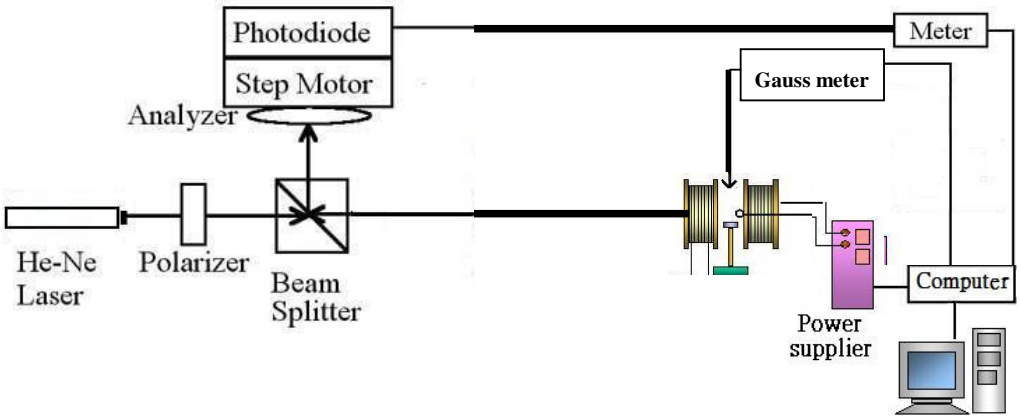

Figure 3 - 11 Schematic illustration of MOKE

3.5 Electron Paramagnetic Resonance (EPR)

The first detection of an EPR signal was studied by Zavoisky in 1945. The simplest possible spectrometer has three essential components: a source of electromagnetic radiation, a sample, and a detector, shown as Fig. 3-5.

To acquire a spectrum, we change the frequency of electromagnetic radiation and measure the amount of radiation which passed through the sample with a detector to observe the spectroscopic absorption. The electromagnetic radiation source and the detector are in a box called the "microwave bridge". The sample is in a microwave cavity, which is a metal box that helps to amplify weak signal from the sample. There is a magnet to "tune" the electronic energy levels. We have a console, which contains signal processing and control electronics and a computer. The computer is used for analyzing data as well as coordinating all the units for acquiring a spectrum.

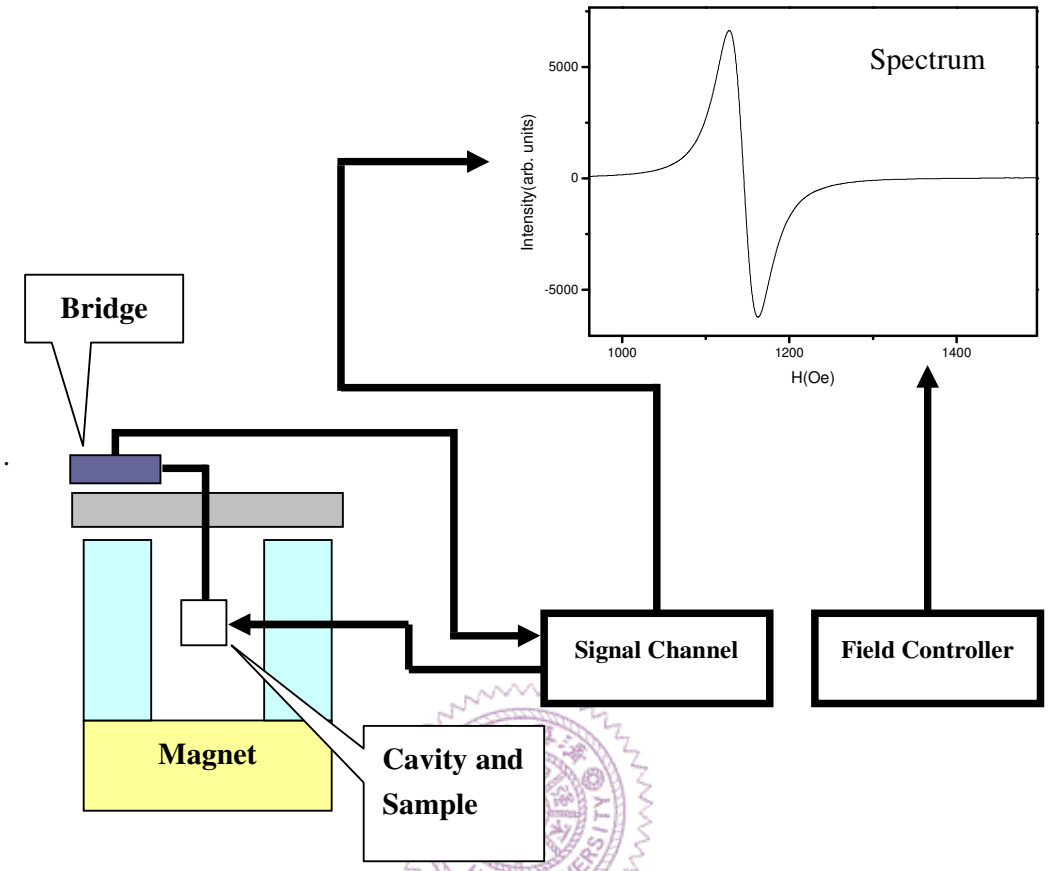

Figure 3 - 12 The layout of electron paramagnetic resonance

3.6 Secondary Ion Mass Spectrometry (SIMS)

SIMS is a technique used to analyze the composition of solid surfaces and thin films by sputtering the surface of the sample with a focused primary ion beam and collecting and analyzing ejected secondary ions. These secondary ions are measured with a mass spectrometer to determine the elemental, isotopic, or molecular composition of the

surface. SIMS is the most sensitive surface analysis technique, being able to detect elements in parts-per-billion range.

A typical SIMS device consists of (1) primary ion gun generating the primary ion beam, (2) a primary ion column, accelerating and focusing the beam onto the sample, (3) high vacuum sample chamber holding the sample and the secondary ion extraction lens, (4) mass analyzer separating the ions according to their mass to charge ratio, (5) ion detection unit. The brief Schematic illustration of SIMS is shown in Fig. 3-6.

SIMS can be used for detecting all elements of the periodic table, and allows the routine measurement of many trace elements at very low concentration. During a measurement, the sample is slowly sputtered away and that is why SIMS is capable of measuring depth profiles and can perform 3-D measurements.

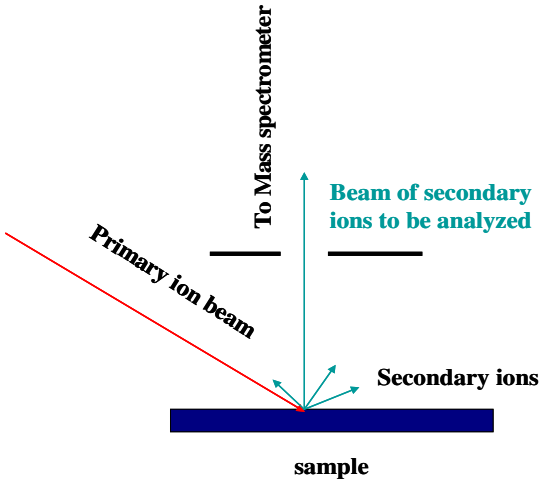

Figure 3 - 13 Schematic illustration of SIMS

3.7 X-ray Magnetic Circular Dichroism (XMCD)

X-ray absorption performed with circularly polarized light predicted by Erskine and Stern in 1975 can supply magnetic information about the initial state of the absorption process. In 1985, Thole et al. show that the lineshape of the $M_{4,5}$ absorption edges of a rare earth ion whose ground state is split by a magnetic field, depends on the relative orientation between the magnetization direction and the polarization vector of the x-rays. X-ray magnetic circular dichroism (XMCD) is a difference spectrum of two x-ray absorption spectra (XAS), one taken with left circularly polarized light, and one with right circularly polarized light. By closely analyzing the XMCD spectrum, information can be obtained on the magnetic properties of the atom. A real explosion of the use of XMCD has followed the development of sum rules by Thole and coworkers. These sum rules, applied to the total absorption and XMCD spectra, allow us to obtain direct values for the orbital and spin moment of the probed atom. The principle of XMCD and the typical spectrum is shown in Fig. 3-7.

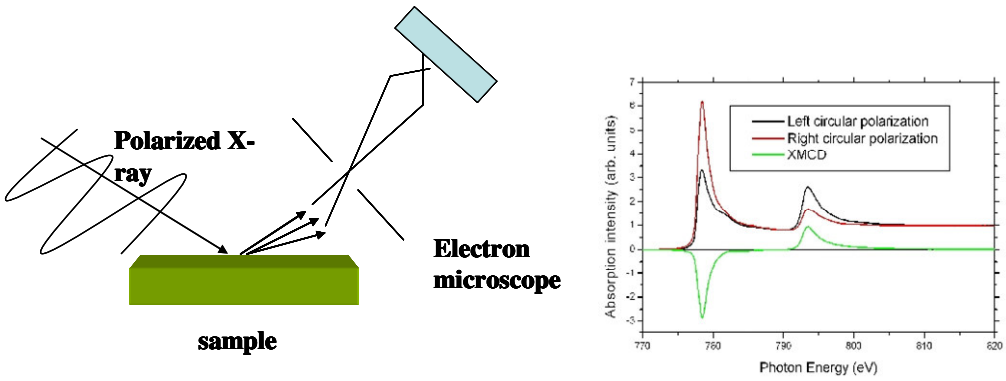

Figure 3 - 14 Schematic illustration of XMCD and typical spectrum

Chapter 4 Results and Discussion

This chapter presents the experimental results and discussions on the half-MTJs that consist of $Co_{60}Fe_{20}B_{20}$ free layer with different capping layers. We have chosen three distinct materials as the capping layer, and measured the magnetic properties, Gilbert damping constant before and after annealing. We used copper as the capping layer for its spin-diffusion length and for suppressing spin-pumping effect[53]. In addition, we also choose MgO as capping layer due to the concept of the dual-barrier MTJ[13]. Because of the lower switching current density observed in dual-barrier MTJ, we have changed the thickness of MgO capping layer, and studied the damping constant, as well as their magnetic properties.

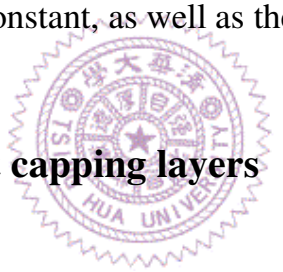

4.1 Effects of different capping layers

4.1.1 Experimental Procedures

All samples were deposited by ITRI without applying external magnetic field through depositions. The annealing treatment was carried out in the 5000 Oe field at set temperature for 2 hours. The film stack for the half-MTJs was SiO_2 / MgO (1 nm) / $Co_{60}Fe_{20}B_{20}$ (2.5nm) / capping material (5 nm) / Ta (5 nm), where the capping material was copper, MgO, or none. The as-deposited free layer was amorphous; even so, the analysis of magnetic properties and the signal of ferromagnetic resonance (FMR) can still be done by vibrating sample magnetometer (VSM) and electron paramagnetic resonance (EPR), respectively. The results of magnetic

properties and FMR are discussed in the following paragraph.

4.1.2 Magnetic Properties

The magnetic properties of three different samples are measured by VSM and the saturation magnetization (Ms), coercivity (Hc) of the samples with different heat treatments are shown in Fig. 4-1 and Fig. 4-2, respectively. From the Ms of the as-deposited state, we observe that the sample with usual Ta capping would have lowest saturation magnetization about 800 emu/cc. It may implied that the sample with the Ta capping layer would induce thin dead layer between CoFeB and Ta caused by Ta intermixing. On the other hand, MgO capping can effectively avoid intermixing. With increasing annealing temperatures, the Ms of the samples with stacks of MgO/CoFeB/Ta and MgO/CoFeB/MgO/Ta increased until 300^{o}C. The increase of saturation magnetization was due to the boron diffusion and the crystallization of CoFeB. As we illustrated in the previous chapter, with decreasing boron concentration, the Ms increases. Furthermore, the amorphous CoFeB would start to be crystallized after high temperature annealing, resulting in the raise of the saturation magnetization. Unlike the other cases, samples with copper capping show the trend that with higher temperature annealing it exhibits lower Ms. The observed results may suggest that copper could suppress the boron diffusion and crystallization of CoFeB. Additionally, copper also caused slight intermixing at the interface and made the Ms decreasing.

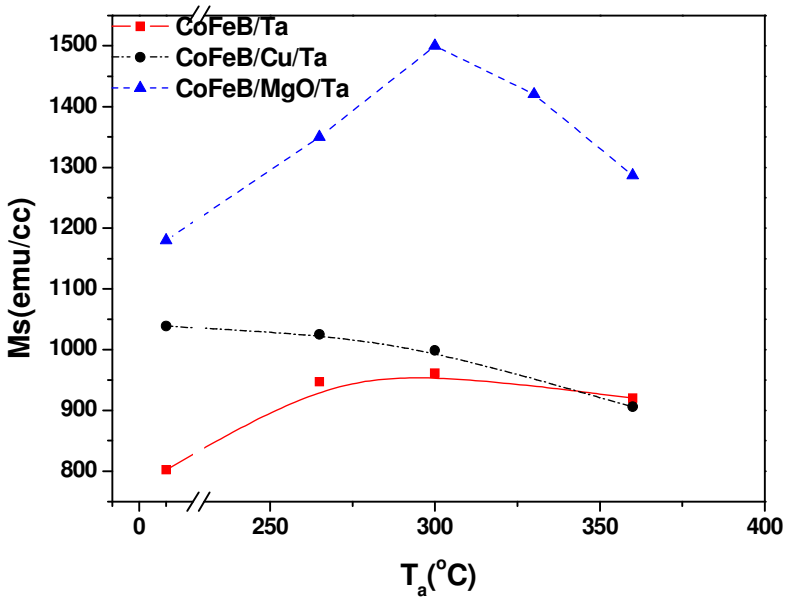

Figure 4 - 3 Ms of samples with different capping layer after distinct annealing

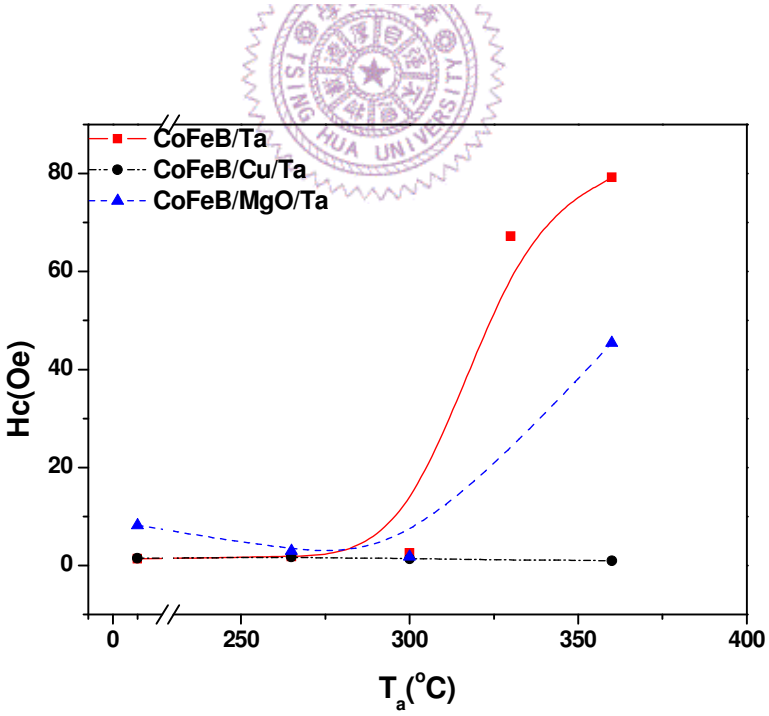

Figure 4 - 4 Hc of samples with different capping layer after distinct annealing

However, after annealing at 360°C, even samples with a MgO capping layer exhibited decreased Ms. We can attribute the drop to the Ta diffusion in the case of only Ta capping. High temperature annealing may enhance the diffusion of Ta and make the dead layer thicker. From the large coercivity of sample with Ta capping after 360°C annealing, we can presume that amorphous CoFeB crystallized completely. Competition between crystallization and intermixing attributes to the larger Ms compared to the as-deposited state. In the case of MgO capping, Ta intermixing is not the reason for the decreasing Ms. The major cause is in connection with oxidation of Co and Fe. The occurrence of CoO_x or FeO_x at the interface between MgO and CoFeB may result in the attenuation[70]. On the other hand, copper capping could really effectively suppress the boron diffusion and then postpone the crystallization[71], that is why we can still observe low coercivity after 360°C annealing.

4.1.3 Gilbert Damping Constant

Ferromagnetic resonance (FMR) was measured by electron paramagnetic resonance equipped with X-Band (9.55 GHz) shown in Fig. 4-3 (a), and TE_{102} cavity, in Fig.4-3 (c). Spectra were acquired by varying the angles (θ_H) between the DC magnetic field and the film plane. The sample was fixed on a rod, and a home-made goniometer, as shown in Fig. 4-3 (b) was used to vary the angle.

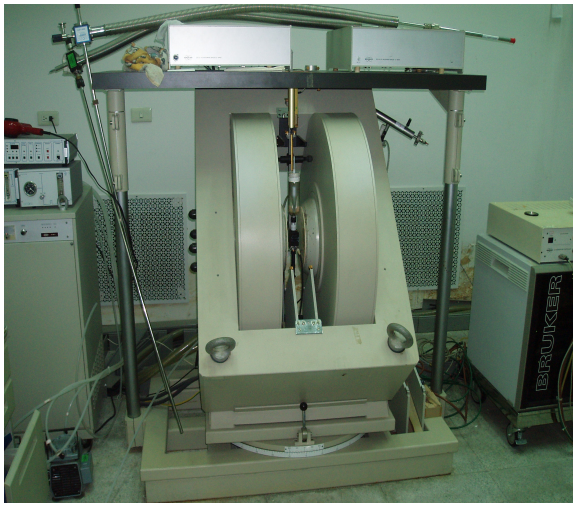

Figure 4 - 3 (d) Electron paramagnetic resonance (ESR)

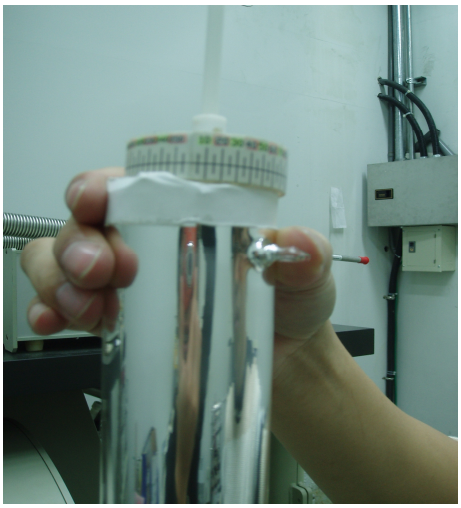

Figure 4 - 3 (e) Home-made goniometer

Figure 4 - 3 (f) X-band microwave

Fig. 4-4 (a) shows the raw data of ferromagnetic resonance spectra with various θ_H. The spectra are the field derivative of absorbed power. The definition of H_R and ΔH_{pp} shown in Fig.4-4 (b) is the field corresponding to the intersection with the base line for the spectrum and the width of field difference between the positive and negative peaks of the spectrum, respectively.

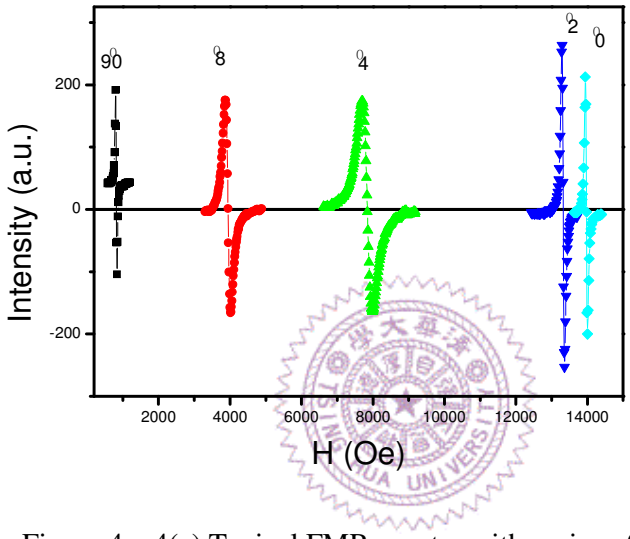

Figure 4 – 4(a) Typical FMR spectra with various θ_H angles

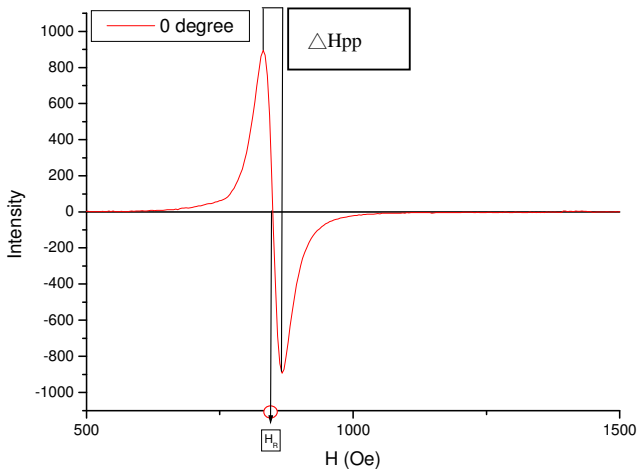

Figure 4 – 4(b) The definition of H_R and ΔH_{pp}

By dealing with the raw data, the angular dependence on H_R and ΔH_{pp} can be obtained in Figure 4-5 (a) and Figure 4-5 (b), respectively. The trend is observed that H_R increases as θ_H and ΔH_{pp} becomes large at the intermediate angle.

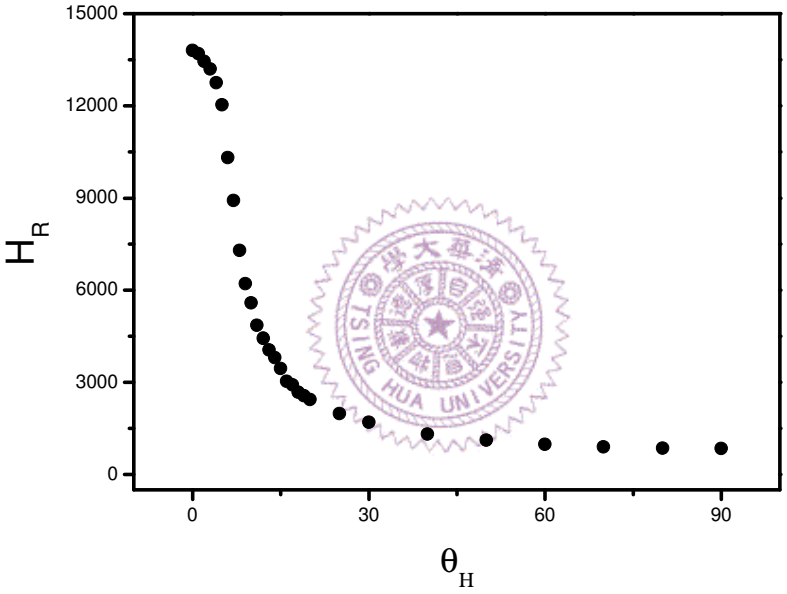

Figure 4 - 5 (c) Angular dependence of FMR resonance field (H_R)

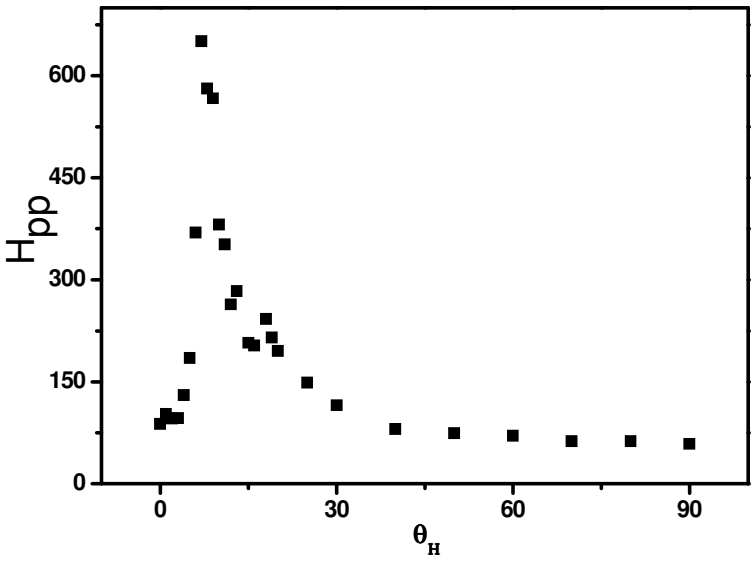

Figure 4 - 5 (d) Angular dependence of FMR linewidth

H_R is a function of θ_H and can be calculated numerically by using eqs. (2.6)-(2.10) with setting the parameter of $4\pi M_{eff.}$ and g-factor.

$$\sin(2\theta_M) = (2H_R / 4\pi M_{eff.}) \sin(\theta_M-\theta_H), \quad (2.6)$$

$$4\pi M_{eff.} = 4\pi Ms-H_{\perp} \quad (2.7)$$

$$\left(\frac{\omega}{\gamma}\right)^2 = H_1 \times H_2 \quad (2.8)$$

$$H_1=H_R \cos(\theta_H-\theta_M) - 4\pi M_{eff.} \cos^2\theta_M \quad (2.9)$$

$$H_2=H_R \cos(\theta_H-\theta_M) - 4\pi M_{eff.} \cos2\theta_M \quad (2.10)$$

One case of best fitting on H_R vs. θ_H, as shown in Fig. 4-6 (a), is calculated by using $4\pi M_{eff.}$ and g-factor of 8.1 kG and 2.122, respectively.

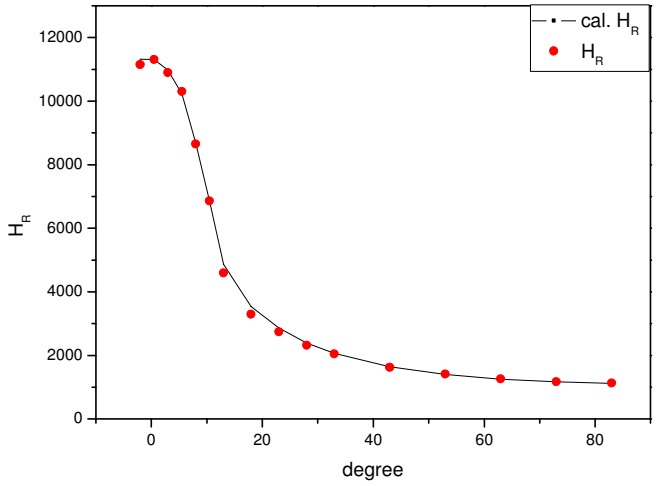

Figure 4 - 6 (c) Angular dependence of FMR resonance field (H_R)

Three components of the intrinsic damping constant, α, the distribution of the effective demagnetization, $\Delta(4\pi M_{eff.})$, and the fluctuation of θ_H, $\Delta\theta_H$, mainly contribute to the peak-to-peak linewidth. Use the eqs. (2.10)-(2.14) along with $4\pi M_{eff.}$ and g-factor of the known value above to fit ΔH_{pp} vs. $\Delta\theta_H$.

$$\Delta H_{pp}^{\alpha} = \frac{1}{\sqrt{3}}\alpha\left(H_1 + H_2\right)\left|\frac{d\left(\frac{\omega}{\gamma}\right)}{dH_R}\right|^{-1} \tag{2.11}$$

$$\Delta H_R = \Delta H_R^{4\pi M_{eff.}} + \Delta H_R^{\theta_H} \tag{2.12}$$

$$\Delta H_R^{4\pi M_{eff.}} = \left|\frac{dH_R}{d\left(4\pi M_{eff.}\right)}\right|\Delta\left(4\pi M_{eff.}\right) \tag{2.13}$$

$$\Delta H_R^{\theta_H} = \left|\frac{dH_R}{d\theta_H}\right| \Delta\theta_H \tag{2.14}$$

$$\Delta H_{pp}^{in\,\mathrm{hom}\,o.} = \left(1/\sqrt{3}\right)\Delta H_R \tag{2.15}$$

The completed results are shown in Fig. 4-6 (b) and the damping constant is obtained.

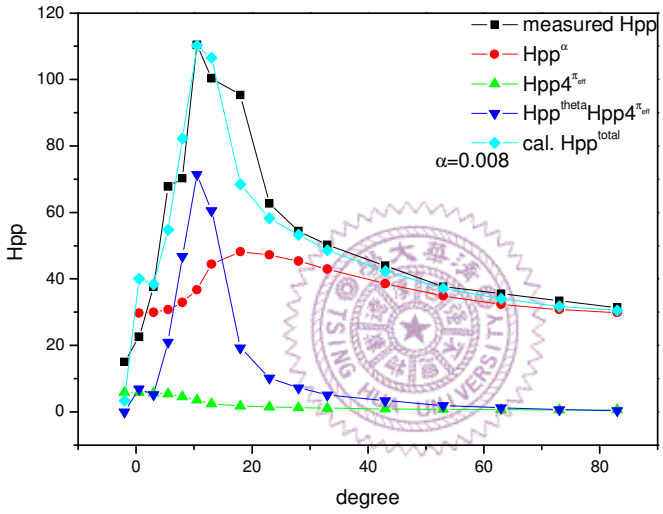

Figure 4 - 6 (d) Angular dependence of FMR linewidth

Through the brief description, we can know the fitting method used in this thesis and then to investigate the capping effects on damping constant which is important for decreasing switching current density of the current-induced switching devices.

Fig. 4-7 illustrates the damping constants (α) of samples with different capping layers and annealing treatment.

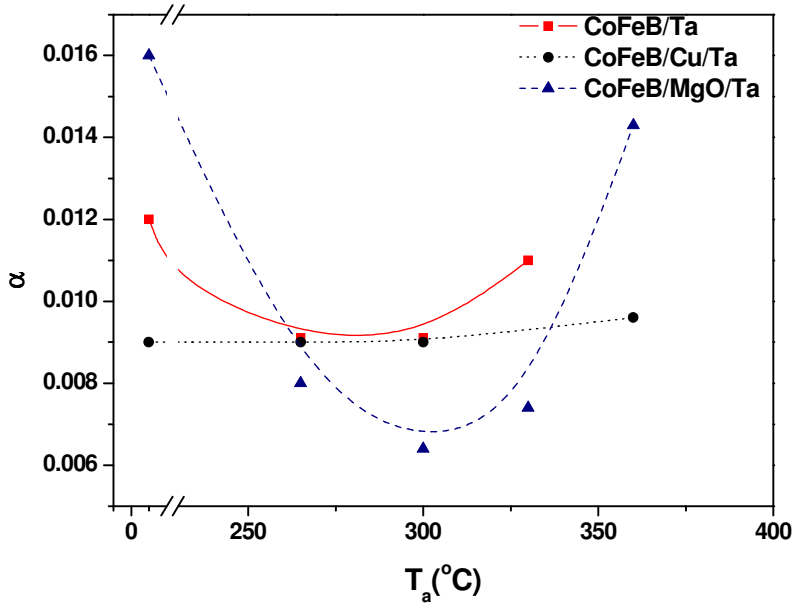

Figure 4 – 7 α of samples with different capping layer after distinct annealing

In the case of samples with Ta capping, we can observe that the damping constant decrease first and then keep at the value of 0.009. The large damping constant for the as-deposited state is due to the intermixing and the spin-pumping effect. After annealing, the diffusion of boron induced decreased damping constants. As we said in the previous chapter, the lower concentration of boron of CoFeB responded to the lower damping constant. The tendency of damping constant of samples with Ta capping agrees with that of Ms. After annealing at 360°C, the absence of the ferromagnetic resonance signal measured by ESR in this case may be due to the anisotropy of spin-orbit coupling and magnetic properties. The large linewidth for the as-deposited samples with MgO capping shows that the oxidation of Co and Fe makes the local magnetization difference. The local distribution would cause interaction of moments and affect the dynamic behavior of moment. With raising annealing temperatures, the

boron diffuses to the interface between MgO and CoFeB and reduces the local oxidation[70]. The reduction not only offers low damping term but also increasing saturation magnetization. It is hard to explain the strange augment of damping constant in the sample with MgO capping after 360°C annealing. The possible reason might be the complete crystallization of CoFeB that brings about disappearance of magnetic anisotropy and cause the incoherent precession. Illustrated in Fig. 4-7, damping constant of the samples with copper capping is independent of the annealing temperature. The unchanging and small damping constant can be attribute to the short spin-diffusion length corresponding to slight spin-pumping effect and the restriction of boron diffusion relating to the decreasing damping constant and decreased Ms. The a little raising α after 360°C annealing comes from the aggravating Cu intermixing.

4.1.4 Depth profile by SIMS

Fig. 4-8 (a) shows the depth profile of Ta in as-deposited state for samples with different capping layer. The amounts of Ta in the CoFeB layer is almost zero for copper and MgO capping cases. However, in the usual Ta capping, even in the CoFeB layer we can observe existence of Ta. This result verifies the occurrence of Ta intermixing in the sample with Ta capping layer.

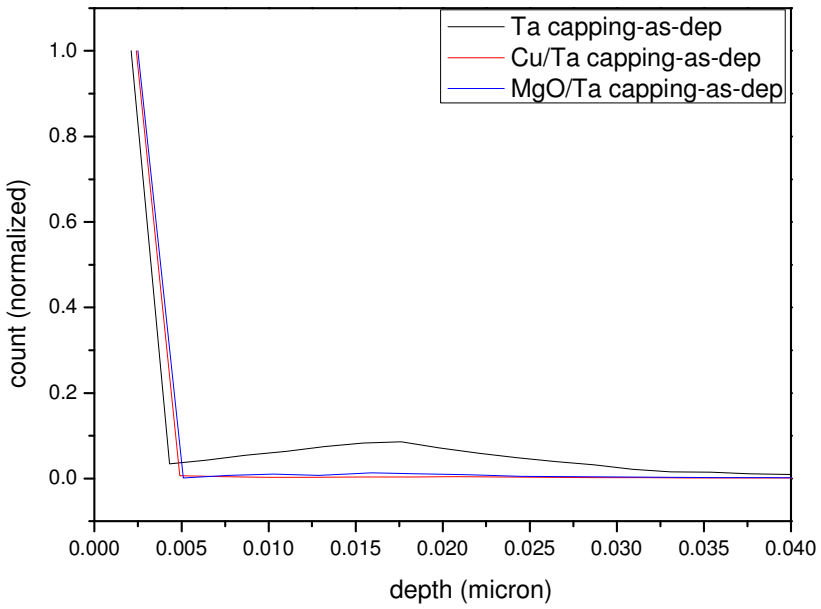

Figure 4 - 8 (e) Depth profile of Ta in as-dep. state samples with different capping

The profiles of boron in as-deposited state are shown in Fig. 4-8 (b). We can confirm that the boron diffusion would not occur in samples without any annealing treatment.

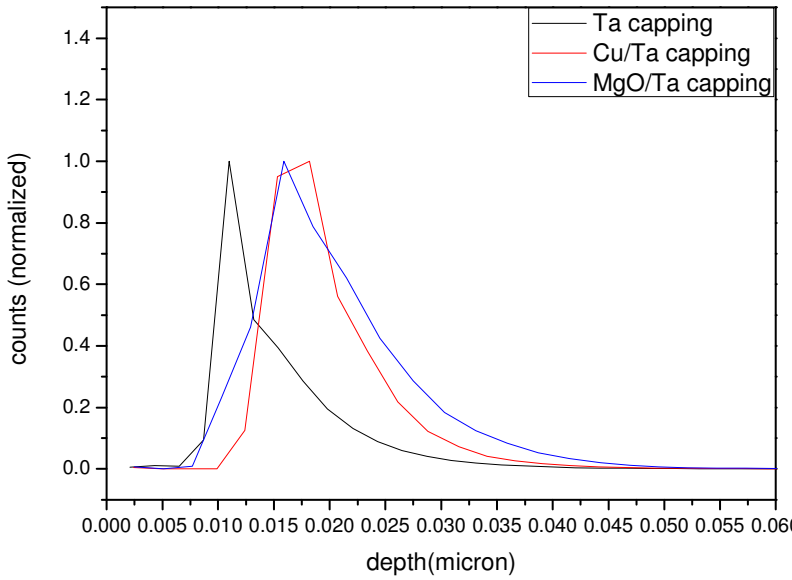

Figure 4 - 8 (f) Depth profile of B in as-dep. state samples with different capping

We have conjectured that the copper capping layer can suppress boron diffusion from the tendency of Ms and α. The depth profiles shown in Fig. 4-8 (c) confirm the conjecture. We can observe that even after high temperature annealing boron is still bridled in the CoFeB region. Copper prevents boron from diffusing out and then keeps the damping constant unchanged.

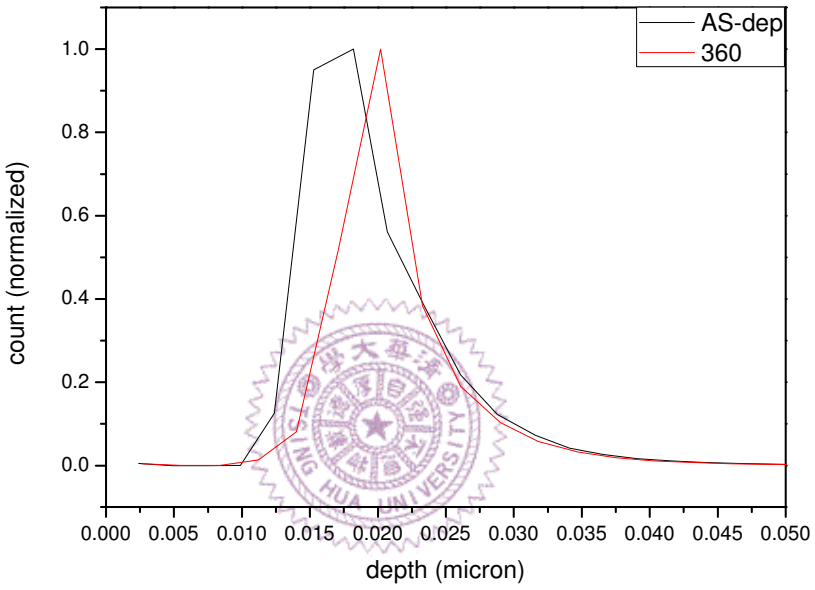

Figure 4 - 8 (g) Depth profiles of B in samples with copper capping

We attributed the decreasing damping constant to the boron diffusing out and the local reduction in the case of MgO capping. Because of the oxidation of boron at the interface between MgO and CoFeB, the concentration of boron would be reduced in CoFeB free layer. The boron oxidation means reduction of CoO_x and FeO_x, so we can see the increasing Ms. The depth profiles illustrated in Fig. 4-8 (d) shows the boron assembling to the top of CoFeB and then verifies our proposition.

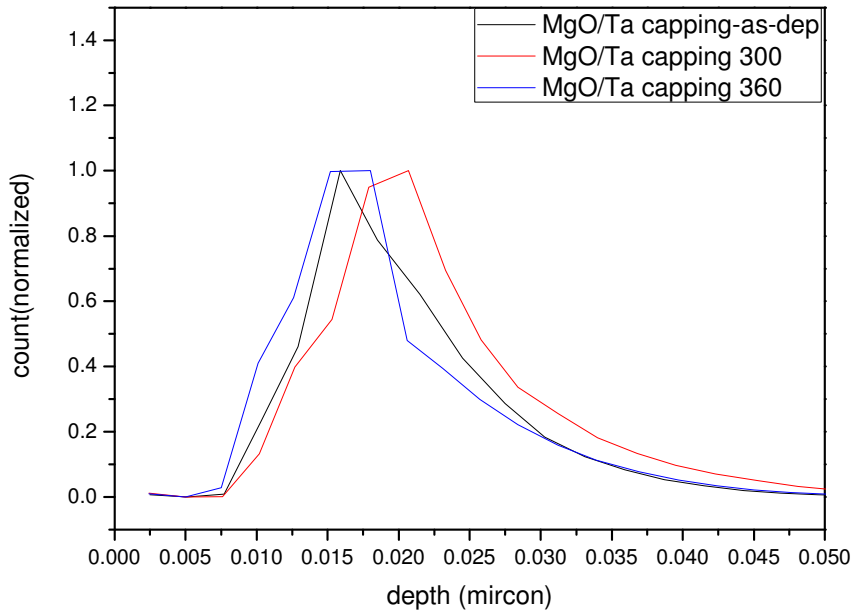

Figure 4 - 8 (h) Depth profiles of B in samples with copper capping

4.1.5 Magnetic properties from XMCD

In the past 15 years the X-ray magnetic circular dichroism (XMCD) spectroscopy has become a powerful tool to investigate an element and site specific manner of the spin and orbital magnetism. The key point is the existence of sum rules which relate the projections $m_{s,\alpha}$ and $m_{l,\alpha}$ of the atomic spin and orbital moments on the propagation direction of the X-rays to the absorption spectra for X-rays with right-circular, left-circular and linear polarization[72].

The XMCD signals of samples of half-MTJ stacks with different capping layer and annealing treatment were measured at the Co $L_{2,3}$ and Fe $L_{2,3}$ edge. From the intensity and shape of the spectrum, we can

analyze the capping effects on magnetic properties of CoFeB. Furthermore, using sum rules to get the atomic moment and ratio of orbital-to-spin magnetic moments is other key point.

The normalized XMCD signals at Co $L_{2,3}$ edge and at Fe $L_{2,3}$ edge of as-deposited samples with Ta capping layer is shown in Fig. 4-9 (a) and Fig. 4-9 (b), respectively.

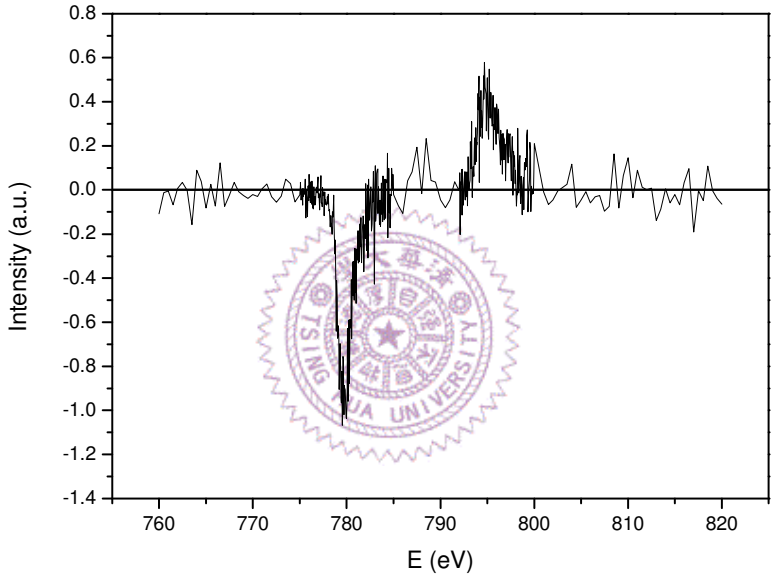

Figure 4 - 9 (c) Normalized XMCD spectrum at Co $L_{2,3}$ edge of as-deposited Sample with Ta capping

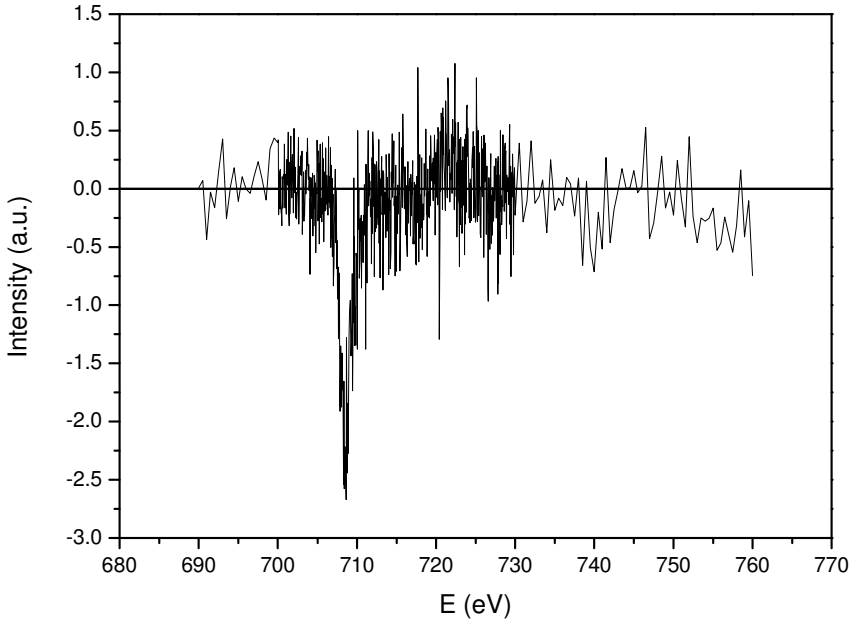

Figure 4 - 9 (d) Normalized XMCD spectrum at Fe $L_{2,3}$ edge of as-deposited Sample with Ta capping

The spectrum at Fe edge is very weak because of the low content of iron in CoFeB.

Fig. 4-10 (a) shows the XMCD spectra of Co signal in the as-deposited samples with Ta capping and MgO capping layer, respectively. From the normalized intensity, we can observe that the XMCD amplitude of the Ta-capped sample is slightly smaller than the amplitude of the MgO-capped one. This effect could be related with the reduction of total Co moment in Ta-capped sample with respect to the MgO-capped one, and in our case the relative decrease of the moment is significantly obvious. However, Fig. 4-10 (b) shows the XMCD spectra of Fe signal for the as-deposited samples with Ta capping and MgO capping layer,

respectively. From the amplitudes of the spectra, we would find the capping effect on total Fe moment is opposite to that on total Co moment.

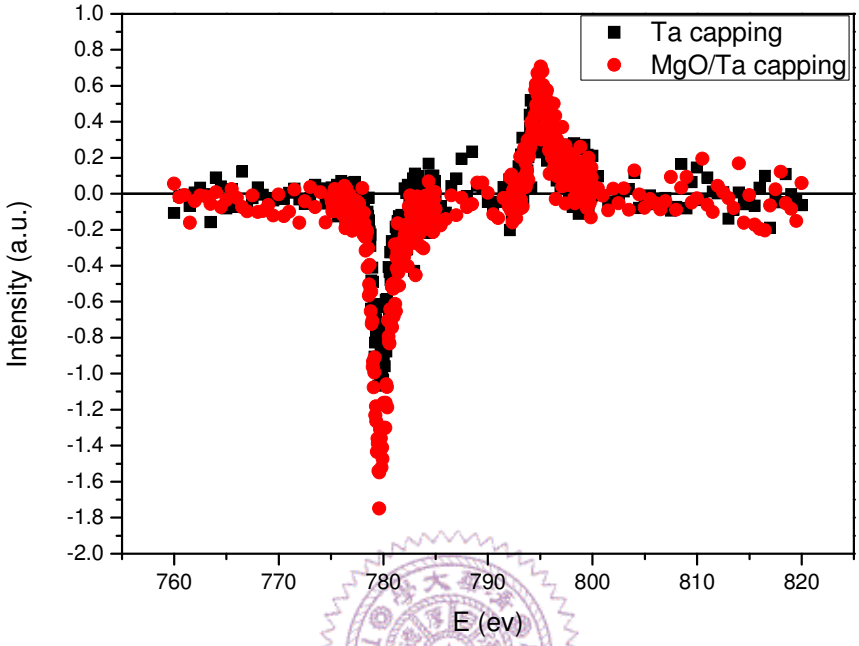

Figure 4 - 10 (c) Normalized XMCD spectra at Co $L_{2,3}$ edge of as-deposited Sample with Ta capping and MgO capping

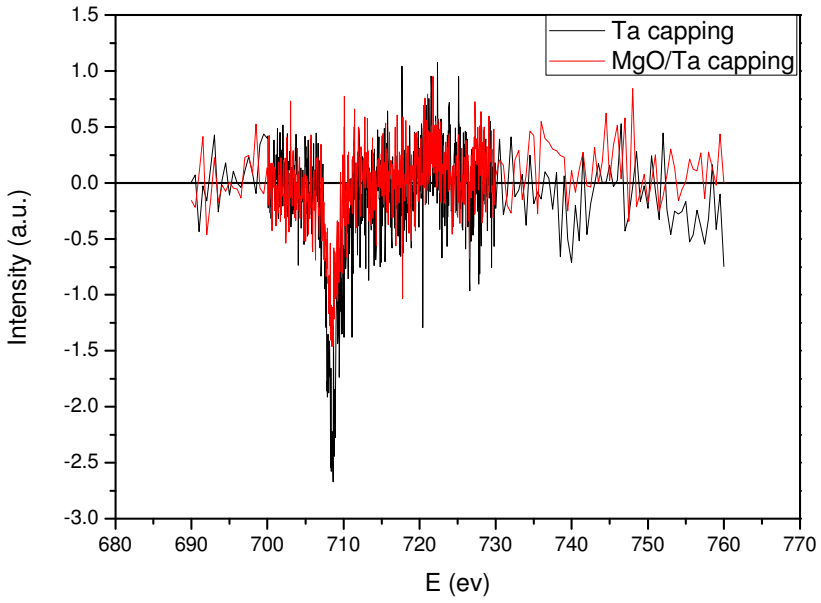

Figure 4 - 10 (d) Normalized XMCD spectra at Fe $L_{2,3}$ edge of as-deposited Sample with Ta capping and MgO capping

Fig. 4-11 shows the XMCD spectra at Co $L_{2,3}$ edge of samples with MgO capping layer after different annealing. As illustrated in this figure, there is a specific small difference between as-deposited state and 300^{o}C annealed samples. However, the spectrum of 360^{o}C annealed sample is dissimilar with the others. We may guess that the configuration of parallel and anti-parallel spin moments is diverse and cases this difference.

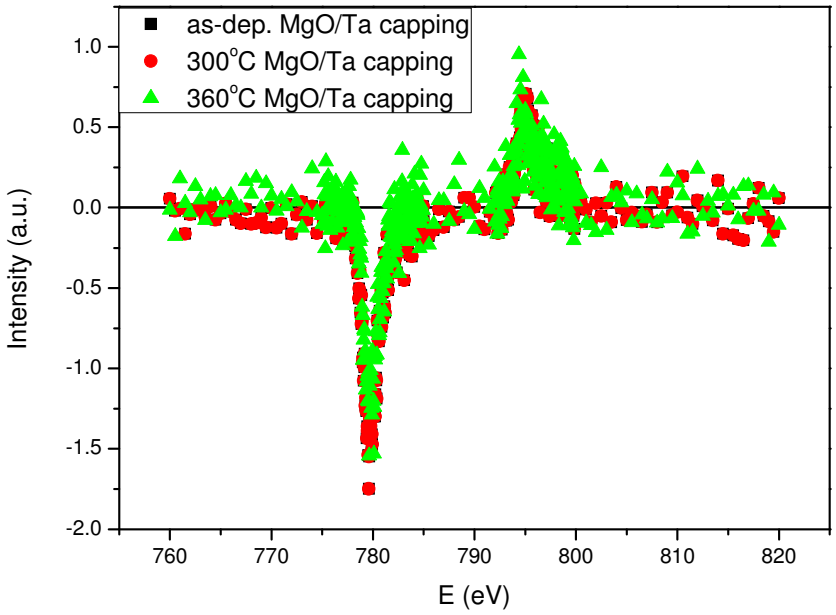

Figure 4 - 11 Normalized XMCD spectra at Co $L_{2,3}$ edge of Samples with MgO capping after different annealing

The integrated XAS signals for samples with MgO capping layer at as-deposited state and 300°C annealed are shown in Fig. 4-12. These integrals are directly related to the number of holes of the Co 3d state, the observed reduction in the annealed sample with respect to the as-deposited state indicates that annealing increases the number of 3d electrons in Co. Applying the XMCD sum rules, we can find the ratio m_L/m_S of orbital-to-spin magnetic moments and the results show in Table 4-1. Through annealing treatment, we can observe the increase of atomic magnetic moment of Co, and the enhanced orbital moment is major contribution.

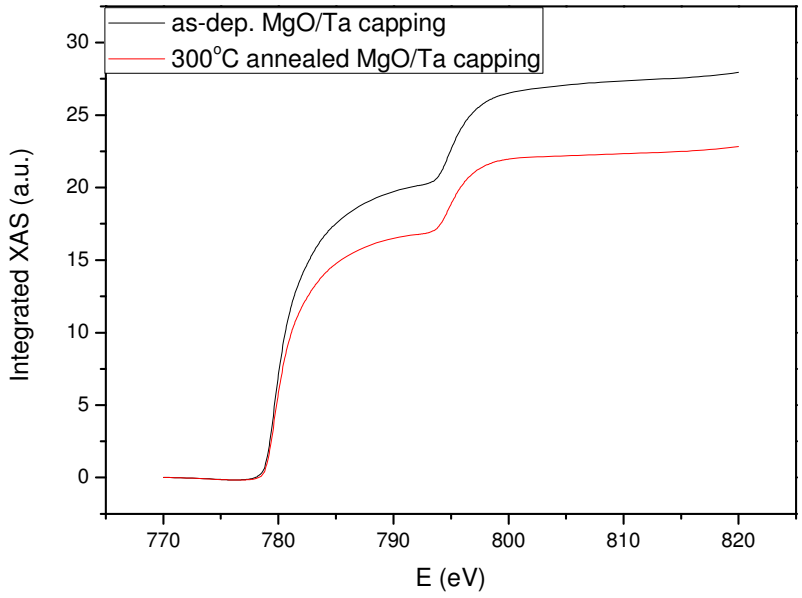

Figure 4 – 12 The integrated XAS signals for samples with MgO capping layer at as-deposited state and 300°C annealed

	M_{orb}	M_{spin}	M_{orb}/M_{spin}	$M_{orb}+M_{spin}$
As-dep.	**0.168**	**1.120**	**0.150**	**1.288**
300°C annealed	**0.332**	**1.415**	**0.234**	**1.747**

Table 4 - 1 The results of applying sum rules for samples with MgO capping layer at as-deposited state and 300oC annealed

4.2 The thickness-dependent effects of MgO capping

4.2.1 Introduction

From the reported experiments of dual-barrier MTJ, we can obtain the appreciably decreased switching current density due to the effects of extra MgO barrier. However, there is a lack of a systemic study on this topic. We would advance some conclusions and report several results in these paragraphs. First, the stacks of the samples are SiO_2 sub/MgO (1nm)/$Co_{60}Fe_{20}B_{20}$ (2.5nm)/MgO (XÅ)/Ta (5nm), where X means various thickness of MgO capping. The MgO capping effects with thickness of 5nm are reported in previous paragraphs. We can observe that with the proper annealing treatment we get the specific low value of damping constant and fine magnetic properties. Nonetheless, 5nm MgO barrier is too thick to be compatible for real MTJs or spintronic devices due to the large resistance. Since the advantages of dual-barrier structure is much attractive and the investigation on this topic is full of interest, we have changed the thickness of MgO capping to study the effects contributed from MgO capping.

4.2.2 Magnetic properties

We mentioned the effects of MgO capping layer for suppressing Ta intermixing in the previous paragraph. To take one step ahead, we changed the thickness of MgO capping layers and observed the trend of

saturation magnetization (Ms) in as-deposited state. The results shown in the Fig. 4-13 inform us that the effect for suppressing intermixing is promoted with increasing MgO thickness in the first place and then saturated. The demarcation for these two steps is that whether the film is continuous or not. When the MgO capping layer is discontinuous, intermixing of Ta would be slacker and slacker with increasing MgO thickness, indicating the increasing Ms. On the other hand, the effect of suppressing intermixing turns to be saturated for continuous MgO films and so is the Ms. For the above-mentioned reasons, We can conjecture that the watershed is 10Å of MgO and we would divide the following discussion into two parts, thinner or thicker than 10Å.

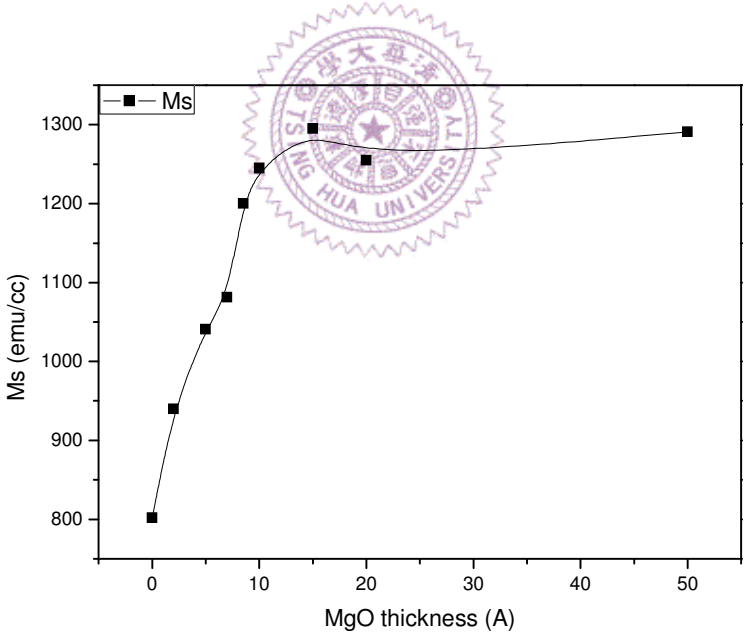

Figure 4 – 13 The as-deposited Ms of samples with different MgO capping thickness

(a) MgO＜10Å

The saturation magnetization of the samples with MgO thickness thinner than 10 Å after different annealing treatment shows in Fig. 4-14. The tendencies are similar and illustrate that the degree of Ta intermixing decreases with increasing MgO thickness. With increasing annealing temperatures, the crystallization of CoFeB would increase and the diffusion of boron should speed up. Increasing Ms with raising annealing temperatures supports our viewpoint. However, the unusual decay of sample without MgO capping after annealing at temperatures higher than 300℃ is due to the serious Ta diffusion.

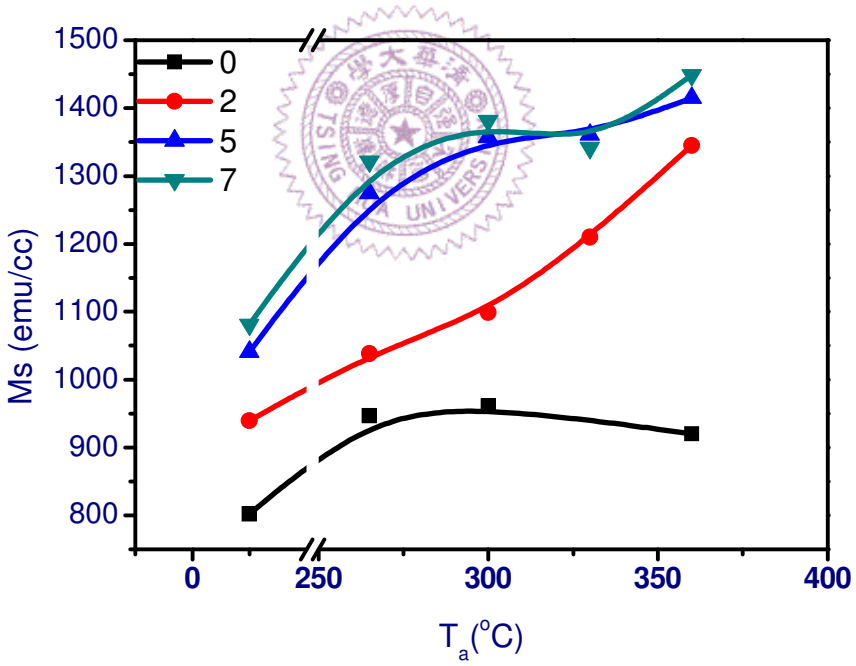

Figure 4 – 14 The Ms of samples with different MgO capping thickness & annealing temperatures

(b)MgO≧10Å

The trends of Ms can be even subdivided into two situations. When the MgO film is continuous and not thick enough, we can observe a little increase of Ms with rising annealing temperatures. On the other hand, thicker MgO capping would induce conspicuous stress on the interface between CoFeB and MgO. Extra stress would complicate the process of crystallization and make the change of Ms hard to explain. To cut a long story short, the extents of CoFeB crystallization and boron diffusion control the tendencies of Ms. The decay appeared in the case of thicker MgO at high temperature annealing is attributed to the local oxidation of Co and/or Fe.

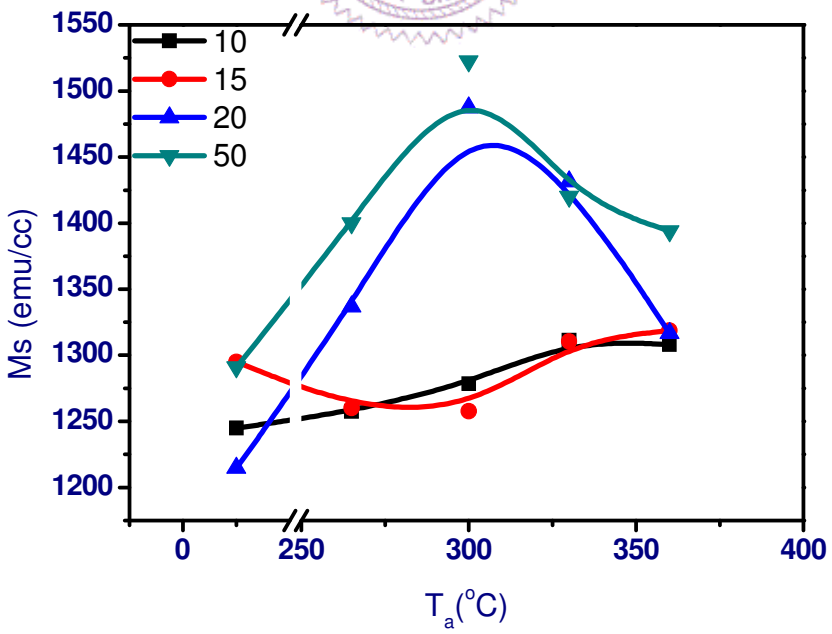

Figure 4 - 15 The Ms of samples with different MgO capping thickness & annealing temperatures

4.2.3 Effective demagnetization and perpendicular anisotropy

The definition of effective demagnetization is $4\pi M_{eff} = 4\pi Ms - H_{\perp}$, where Ms is the saturation magnetization and $H_{\perp}$ is the perpendicular anisotropy. The two terms $4\pi M_{eff}$ and $H_{\perp}$ can be extracted from the FMR signal by fitting the angular H_R spectra.

(a) MgO < 10Å

Fig. 4-16 (a) and 4-16 (b) are effective demagnetization and perpendicular anisotropy of samples with different annealing temperatures, respectively. The behavior of $4\pi M_{eff}$ is hard to be concluded because of the influence from two aspects. The total perpendicular anisotropy of a sample is any anisotropy with a symmetry axis along the film normal. Fluctuations in magnetization and in thickness would affect this anisotropy. Illustrated in Fig. 4-16 (b), thinner film would make the interface rougher and then increase the anisotropy after annealing because of the local mixing and boron diffusion.

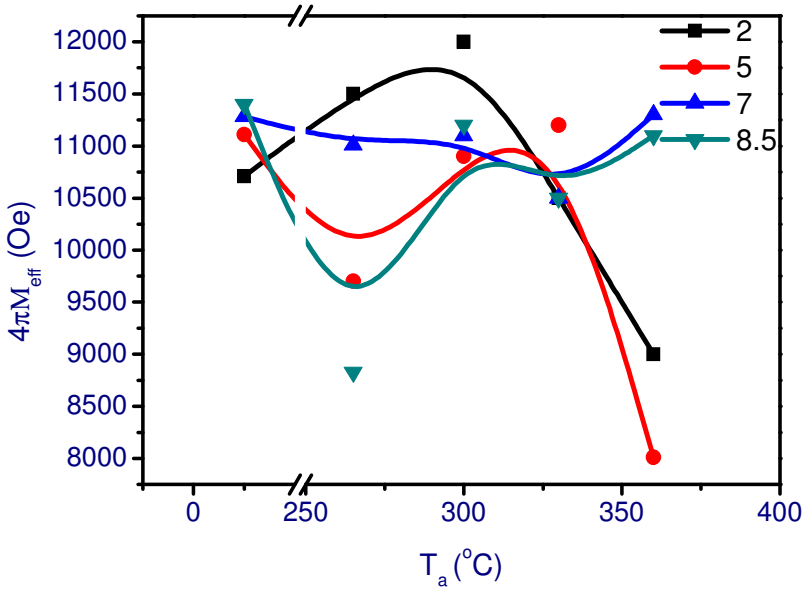

Figure 4 -16 (c) The effective demagnetization of samples with different MgO capping thickness & annealing temperatures

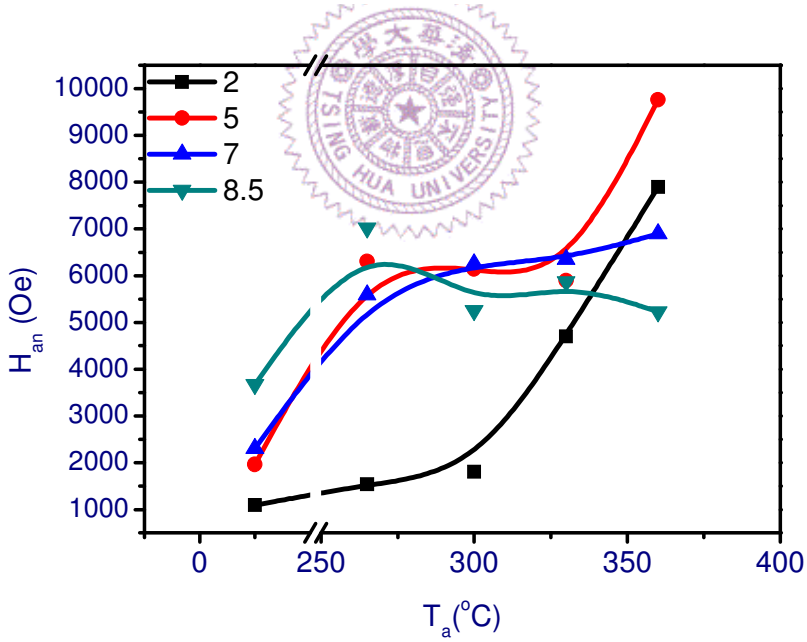

Figure 4 -16 (d) The perpendicular anisotropy of samples with different MgO capping thickness & annealing temperatures

(b)MgO≧10Å

We still can subdivide these cases into two parts. If the MgO film is continuous and not thick enough, the anisotropy do not show remarkable change with annealing temperatures, shown in Fig. 4-17 (b). However, the anisotropy is roughly increasing with raising thickness. The enhanced anisotropy may be induced by the stress caused by MgO capping layer. Furthermore, higher annealing temperatures can leads in stress relaxation and smooth interface contributing to reduction of $H_{\perp}$. The results of effective demagnetization illustrated in Fig. 4-17 (a).

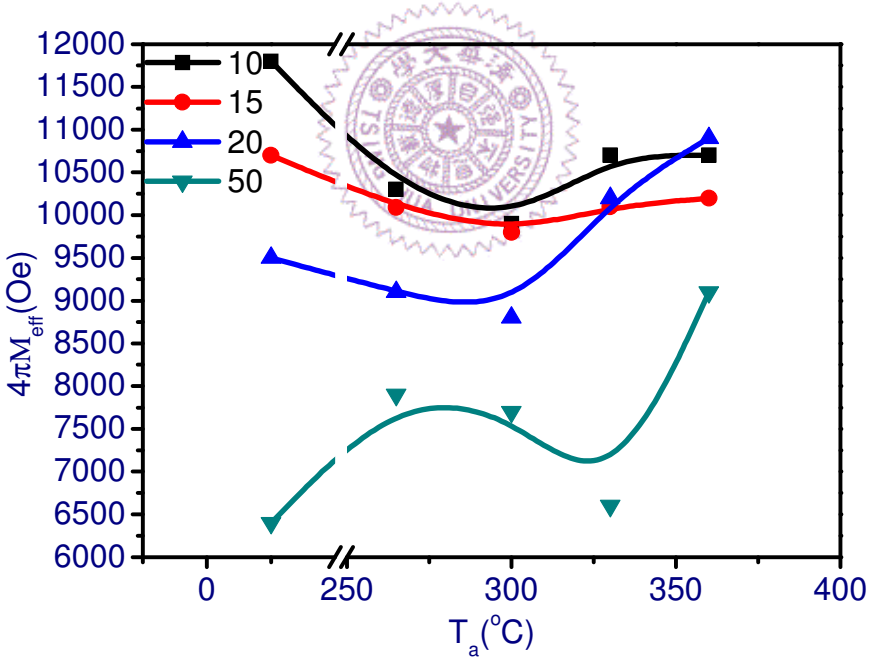

Figure 4 - 17 (b) The effective demagnetization of samples with different MgO capping thickness & annealing temperatures

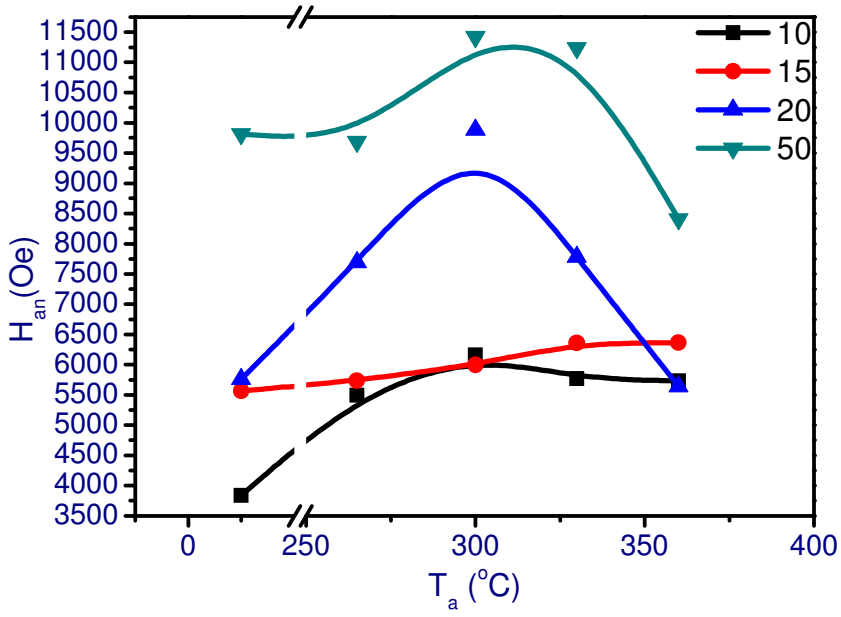

Figure 4-17 (b) The perpendicular anisotropy of samples with different MgO capping thickness & annealing temperatures

4.2.4 g factor

The g factor is related to the spin-orbit interaction, which reflects the lattice motions. The value of g-factor of free electron is about 2.0, and the deviation means the existence of interaction. Large deviation of g factor indicates large damping. In other words, higher contribution of orbital moment shows strong interaction with lattice and larger damping. In a word, we can roughly know the damping term from the values of g factor.

(a) MgO＜10Å

The trends of g factor shown in Fig. 4-18 give us some hints on how the damping changing with annealing temperatures. Based on the concept of deviation of g-factor, we can expect that the damping

constant changes a little with annealing temperatures in cases of thicker MgO capping. However, in the thinner cases high annealing temperatures enhance increase of damping.

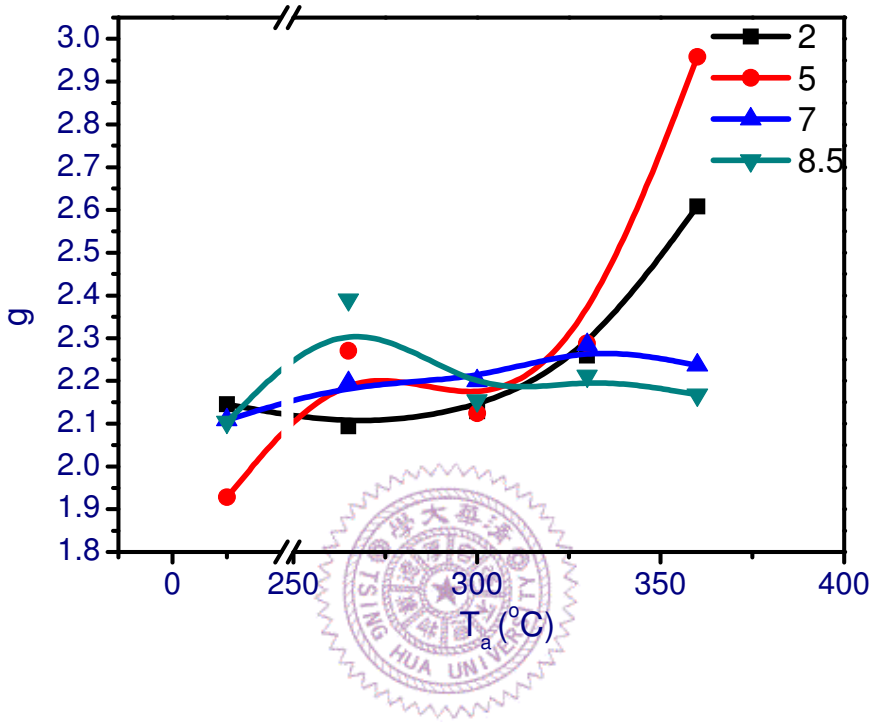

Figure 4 -18 The g-factor of samples with different MgO capping thickness & annealing temperatures

(b)MgO≧10Å

The almost constant g values in the cases of continuous MgO films shown in Fig. 4-19 represent the steadfast damping constant, except for the thickest case. The specific thick MgO capping layer may cause obvious change of composition at the interface or structure after annealing treatment.

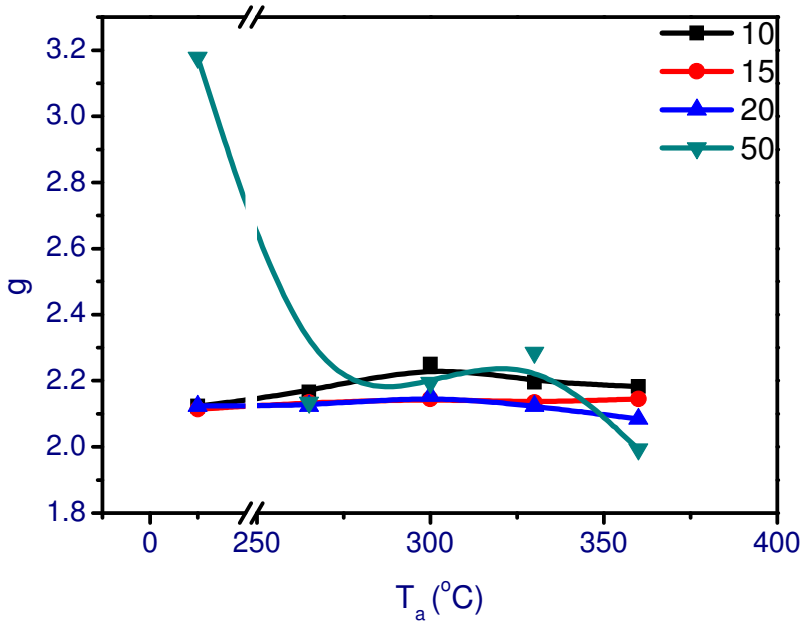

Figure 4 – 19 The g-factor of samples with different MgO capping thickness & annealing temperatures

4.2.5 Damping constant vs. deviation of g-factor

The intrinsic damping term G is roughness proportional to $(g-2)^2$. We would compare our fitting results with the rough parameter $(g-2)^2$ in this paragraph.

(a) MgO＜10Å

Fig. 4-20 (a)-(d) show the comparison of deviation of g-factor and our fitting result. The tendencies of these two curves in the cases of thinner MgO capping are similar, indicating that the chief contribution to damping is the simple lattice motion. Our fitting results are the effective damping constant, not intrinsic term. When the MgO thickness is equal to 8.5Å, we can observe very different trends. The

dissimilarity means some other contribution for damping mechanism except spin-orbit coupling, such as two-magnon interaction.

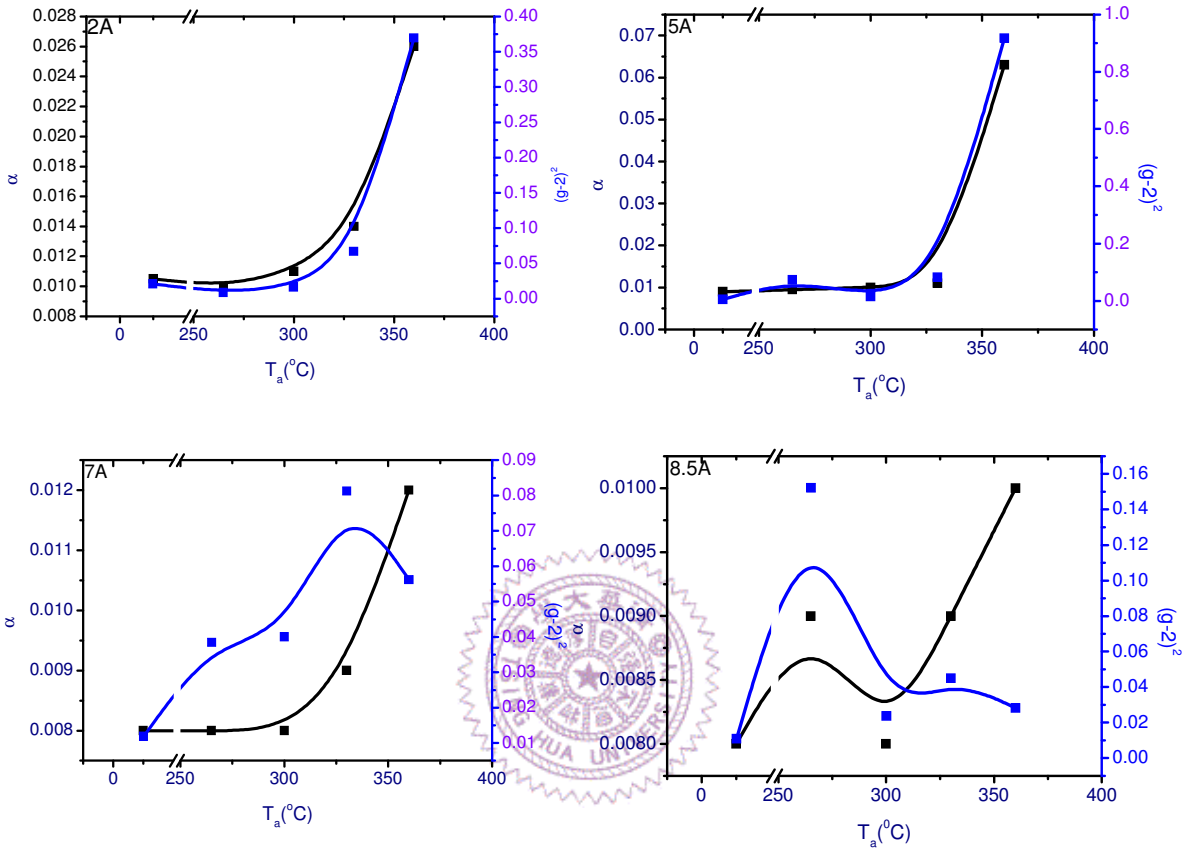

Figure 4 - 20 (a)-(d) The comparison of our fitting damping constant and $(g-2)^2$ for samples with different MgO capping thickness & annealing temperatures

(b)MgO≧10Å

The trends shown in Fig. 4-21 (a)-(d) are very different, indicating that the factors affecting damping behavior are complex in the continuous capping films, especially after annealing.

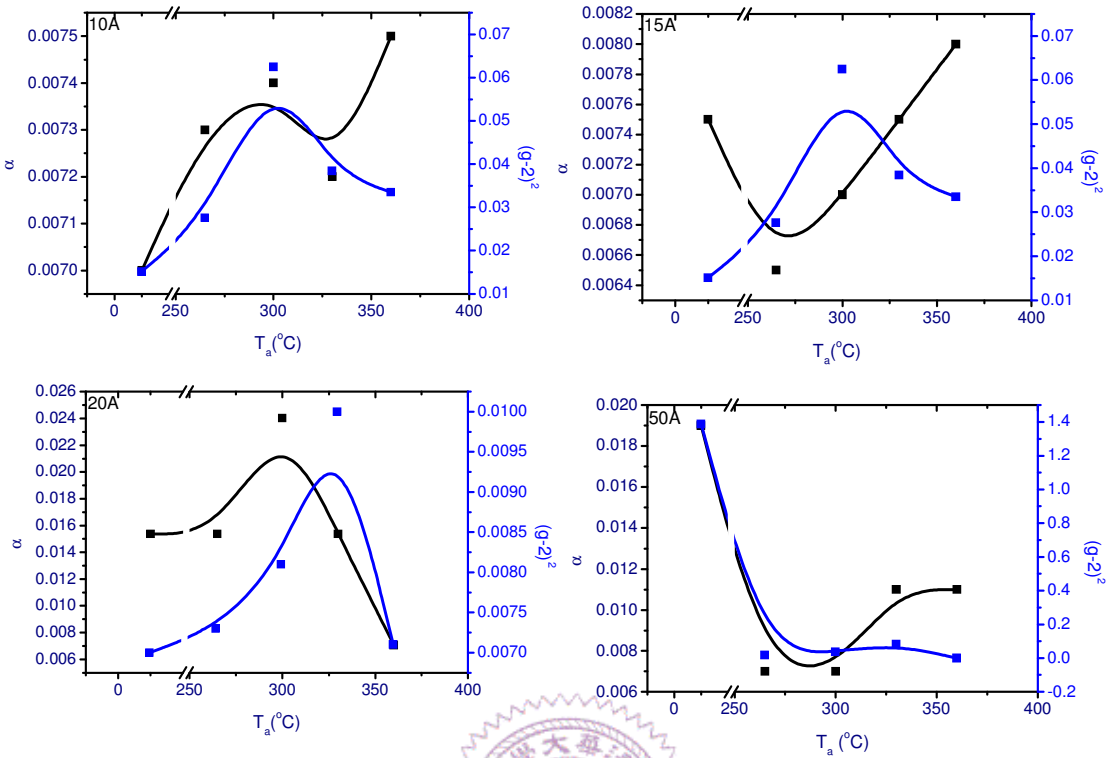

Figure 4 - 21 (a)-(d) The comparison of our fitting damping constant and $(g-2)^2$ for samples with different MgO capping thickness & annealing temperatures

4.2.6 Damping constant

Because of the complex factors influencing damping constants, we would subdivide the following discussion into four parts for clear explanation.

(a) Discontinuous MgO

Fig. 4-22 (a)-(c) show the tendencies of damping constant in the cases of MgO=2Å, 5Å and 7Å, respectively. Intermixing of Ta would make the as-deposited damping constant large. With increasing annealing temperatures, boron diffusion and crystallization of CoFeB

decrease α. The balance of these effects determines the trends. However, at high annealing temperature the serious Ta diffusion increases the damping emphatically.

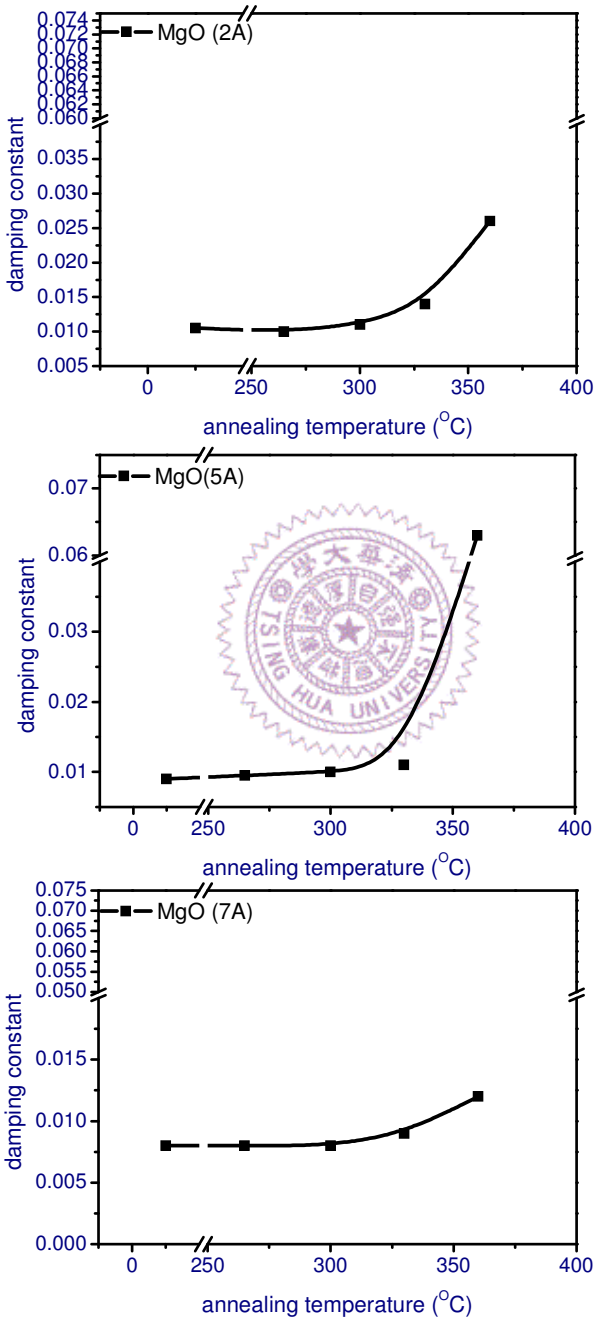

Figure 4 - 22 (a)-(c) Our fitting damping constants for samples with different MgO capping thickness & annealing temperatures

(b) Transition between discontinuous and continuous

Fig. 4-23 shows the change of α with different annealing temperatures in the case of MgO thickness in the transition region. We observe that the fluctuation of anisotropy and magnetization, even the existence of two-magnon interaction result in the oscillation of damping constant.

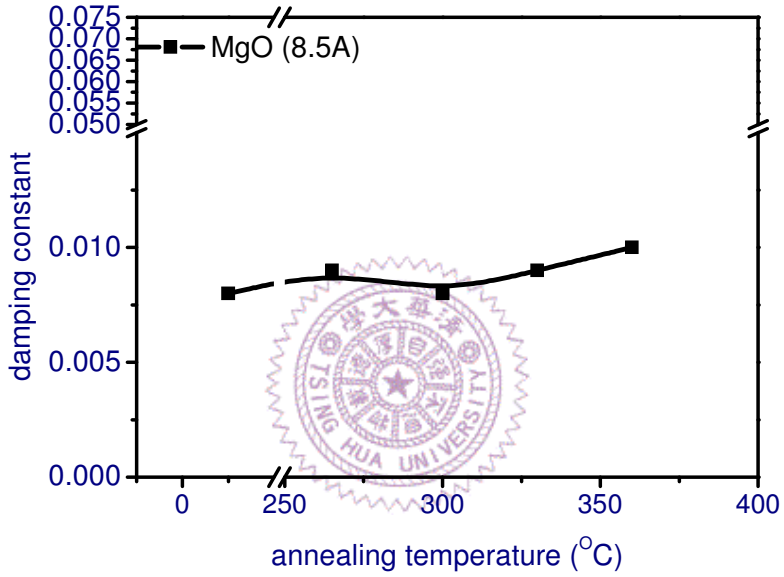

Figure 4 – 23 Our fitting damping constants for samples in the transition region with different annealing temperatures

(c) Continuous MgO capping

When the MgO capping layer becomes continuous and not too thick, we would observe smoother and sharper interface between MgO and CoFeB, namely low α. On the other hand, the boron diffusion and suppressing intermixing keep damping constants unchanged, even at high annealing temperature. In short, we can get the low and stationary value of effective damping shown in Fig. 4-24 (a)-(b).

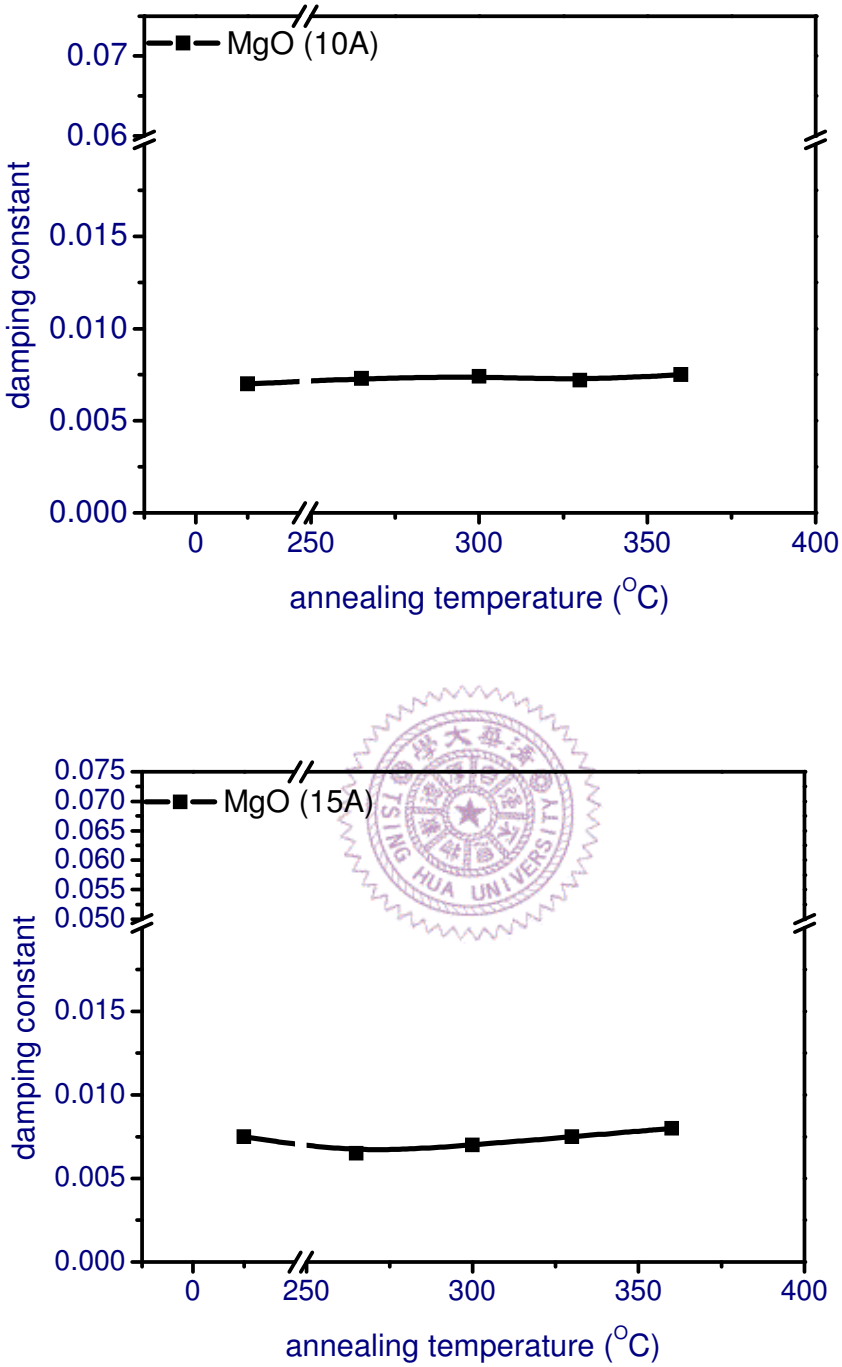

Figure 4 – 24 (a)-(b) Our fitting damping constants for samples with continuous MgO capping after different annealing temperatures

(d) Extremely thick MgO capping

This case shown in Fig. 4-25 is the same as the situation illustrated in part one of this chapter. The large damping constant of as-deposited state is due to the interfacial oxidation. With increasing annealing temperatures, the boron diffusion reducing CoO_x/FeO_x and crystallization of CoFeB would lower the damping constant. Damping parameters raise again because of local oxidation and roughness.

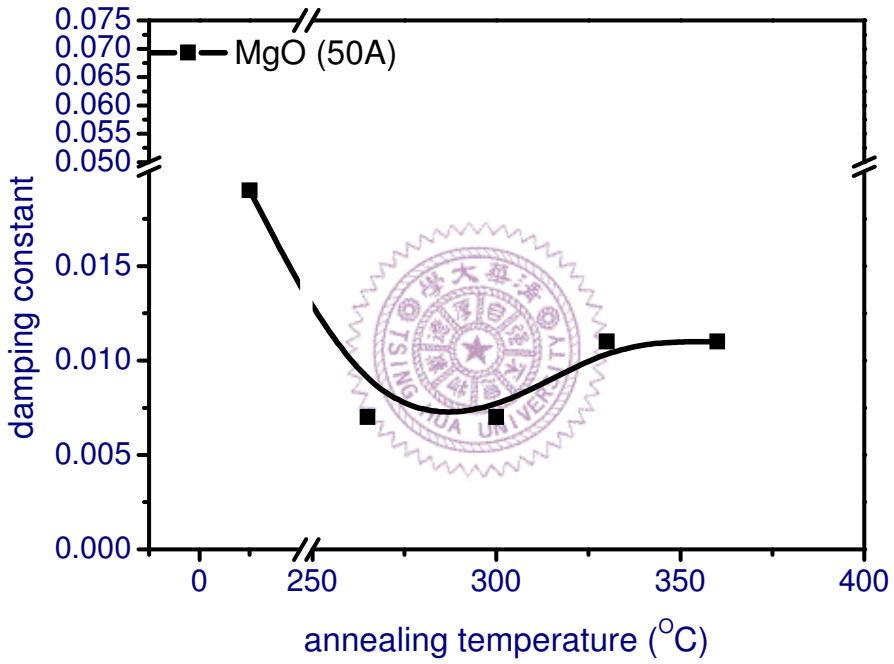

Figure 4 – 25 Our fitting damping constants for samples with extremely thick MgO capping after different annealing temperatures

Chapter 5 Conclusions

In this dissertation, we have firstly investigated the effects of different capping layer on the properties of amorphous CoFeB for MTJs. To analyze the damping constants of this ferromagnet with different capping materials and heat treatment, we utilized the angular dependence of ferromagnetic resonance technique.

We observed that when the effect of intermixing exists in the as-deposited state, it would form dead layers and decrease the saturation magnetization. Furthermore, the large damping constant reflects this intermixing. On the other hand, the samples with copper capping layer suppress the spin-pumping effect and result in low damping constant. However, the MgO capping layer would amount to local oxidation and initial larger damping constant. With annealing, the diffusion of boron and increasing crystallization of CoFeB make damping constant lower and saturation magnetization higher. In terms of trends of damping constant, we can surmise that the Cu capping layer would suppress the boron diffusion and lead to unchanged damping parameters.

Subsequently, in light of the low switching current density of dual-MgO MTJs, we have systematic studies on the half-MTJ structures with extra MgO capping layer. By changing the thickness of MgO capping layer and using various annealing, we can get the low damping constant and the fine magnetic properties with proper thickness of MgO

and annealing temperature.

The observation of low damping constant is induced by the interaction at the interface. Tuning this parameter, we should obtain the appropriate switching current density and switching behavior for spin-transfer devices.

References

[1] Y. Huai et al., Jpn. J. Appl. Phys. **45**, 3835-3841 (2006)

[2] J. C. Slonczewski, J. Magn. Magn. Mater. **159**, L1 (1996)

[3] L. Berger, Phys. Rev. B **54**, 9353 (1996)

[4] J. Z. Sun, Phys. Rev. B **62**, 570 (2000)

[5] D. M. Apalkov et al., Phys. Rev. B **72**, 180405 (2005)

[6] Z. Li et al., Phys. Rev. B **69**, 134416 (2004)

[7] E. B. Myers et al., Phys. Rev. Lett. **89**, 196801 (2002)

[8] Y. Huai et al., Appl. Phys. Lett. **84**, 3118 (2004)

[9] M. Pakala et al., J. Appl. Phys. **98**, 056107 (2005)

[10] Z. Diao et al., Appl. Phys. Lett. **87**, 232502 (2005)

[11] H. Kubota et al., Jpn. J. W. Appl. Phys. **44**, L1237 (2005)

[12] J. Hayakawa et al, Jpn. J. Appl. Phys. **44**, L1267 (2005)

[13] Y. Huai et al., Appl. Phys. Lett. **90**, 132508 (2007)

[14] W. H. Butler et al., Phys. Rev. B **63**, 054416 (2001)

[15] Y. Huai et al., IEEE Trans. Magn. **40**, 2269 (2005)

[16] Mathon, J., Phys. Rev. B **63**, 220403 (2001)

[17] S. Yuasa et al., Nat. Mater. **3**, 868 (2004)

[18] Stuart S. P. Parkin et al., Nat. Mater. **3**, 862 (2004)

[19] X.-G. Zhang et al., Phys. Rev. B **70**, 172407 (2004)

[20] S. Yuasa et al., Appl. Phys. Lett. **89**, 042505 (2006)

[21] E. C. Stoner et al., Philos Trans. R. Soc. Assoc. **240**, 599 (1948)

[22] F. E. Luborsky, Amorphous Metallic Alloys, Butterworths, London (1983)

[23] R. C. O'Handley, Modern Magnetic Materials, Wiley, New York (2000)

[24] Y. K. Kim, J. Magn. Magn. Mater. **304**, 79-82 (2006)

[25] Y. Miura et al., Phys. Rev. B **69**, 144413 (2004)

[26] P. J. Webster, J. Phys. Chem. Solid **32**, 1221 (1971)

[27] David D. Djayaprawira et al., Appl. Phys. Lett. **86**, 092502 (2005)

[28] Y. M. Lee et al., Appl. Phys. Lett. **89**, 042506 (2005)

[29] J. Y. Bae, J. Appl. Phys. **99**, 08T316 (2006)

[30] X.-G. Zhang et al., Phys. Rev. B **68**, 092402 (2003)

[31] J. Hayakawa et al., Appl. Phys. Lett. **89**, 232510 (2006)

[32] K. Tsunekawa et al., Jpn. J. W. Appl. Phys. **45**, L1152 (2006)

[33] S. Yuasa et al., Appl. Phys. Lett. **87**, 242503 (2005)

[34] K. Tsunekawa et al., IEEE Trans. Magn. **42**, 103 (2006)

[35] M. Oogane et al., Jpn. J. W. Appl. Phys. **45**, 3889 (2006)

[36] L. Landau et al., Phys. Z. Sowjetunion **8**, 153 (1935)

[37] K. Takano, IEEE Trans. Magn. **40**, 257 (2004)

[38] D. Suess et al., J. Magn. Magn. Mater. **290**, 518-521 (2005)

[39] J.-G. Zhu et al., IEEE Trans. Magn. **42**, 2739-2742 (2006)

[40] J. Z. Sun, J. Magn. Magn. Mater. **202**, 157 (1999)

[41] J. Z. Sun, Phys. Rev. B **62**, 570 (2000)

[42] S. Mangin et al., Nature Mater. **5**, 210 (2006)

[43] J.-G. Zhu et al., IEEE Trans. Magn. **43**, 2349 (2006)

[44] S. Chikazumi, Physics of Ferromagnetism, Oxford Uni. Press, Oxford (1995)

[45] Y. Shimizu et al., J. Appl. Phys. **81**, 4513 (2000)

[46] D. Suess et al., J. Appl. Phys. **99**, 08B902 (2006)

[47] H. Jaffres et al., Phys. Rev. B **67**, 174402 (2003)

[48] J. Z. Sun et al., Phys. Rev. Lett. **92**, 088302 (2004)

[49] H. Suhl, IEEE Trans. Magn. **34**, 1834 (1998)

[50] V. Kamberský, Can. J. Phys. **48** 2906 (1970)

[51] Y. Ando et al., J. Magn. Magn. Mater. **239**, 42 (2002)

[52] Y. Ando et al., Phys. Rev. B **66**, 104413 (2002)

[53] G. E. W. Bauer et al., Phys. Rev. Lett. **88**, 117601 (2002)

[54] G. E. W. Bauer et al., Phys. Rev. B **66**, 224403 (2002)

[55] T. Taniguchi et al., Phys. Rev. B **76**, 092402 (2007)

[56] Griffiths J-H-E, Nature **158**, 670 (1946)

[57] Kittel C, Phys. Rev. **71**, 270 (1947)

[58] B. Heinrich et al., Phys. Rev. Lett. **59**, 1756 (1987)

[59] S. Mizukami et al., Jpn. J. W. Appl. Phys. **40**, 580-585 (2006)

[60] H. Shul, Phys. Rev. **97**, 555 (1955)

[61] C. Chappert K, Phys. Rev. B **34**, 3192 (1986)

[62] D. L. Mills et al., Phys. Rev. B **68**, 060102 (2003)

[63] Y. Ando et al., J. Appl. Phys. **101**, 09C106 (2007)

[64] P.C. Fannin et al., J. Magn. Magn. Mater. **299**, 425-429 (2006)

[65] Kittel C, Phys. Rev. **73**, 155 (1947)

[66] Farle M, Rep. Prog. Phys. **61**, 755 (1998)

[67] Buchmeier M et al., J. Phys.: Condens. Matter **15**, S443 (2003)

[68] Y. Ando et al., Jpn. J. Appl. Phys. **40**, 580-585 (2001)

[69] J Lindner et al., J. Phys.: Condens. Matter **15**, S465 (2003)

[70] J. C. Read et al., Appl. Phys. Lett. **90**, 132503 (2007)

[71] D. J. Kim et al., J. Appl. Phys. **101**, 09B505 (2007)

[72] James W. et al., J. Electron. Spectrose. Relat. Phenom. **130**, 97-100 (2003)